Spectral Clustering en IRM de diffusion pour Retrouver les Faisceaux de la Matière Blanche

Demian Wassermann, Maxime Descoteaux, Rachid Deriche

INSTITUT NATIONAL DE RECHERCHE EN INFORMATIQUE ET EN AUTOMATIQUE

Recovering cerebral white matter structures with Spectral Clustering of Diffusion MRI Data

Demian Wassermann, Maxime Descoteaux and Rachid Deriche

N° 6351

November 2007

Thème BIO

ISSN 0249-6399 ISRN INRIA/RR--6351--FR+ENG

Recovering cerebral white matter structures with Spectral Clustering of Diffusion MRI Data

Demian Wassermann, Maxime Descoteaux and Rachid Deriche

Thème BIO — Systèmes biologiques

Projets Odyssée

Rapport de recherche n° 6351 — November 2007 —52 pages

Abstract: White matter fiber clustering allows to get insight about anatomical structures in order to generate atlases, perform clear visualizations and compute statistics across subjects, all important and current neuroimaging problems. In this work, we present a Diffusion Maps clustering method applied to diffusion MRI in order to cluster and segment complex white matter fiber bundles. It is well-known that Diffusion Tensor Imaging (DTI) is restricted in complex fiber regions with crossings and this is why recent High Angular Resolution Diffusion Imaging (HARDI) such has Q-Ball Imaging (QBI) have been introduced to overcome these limitations. QBI reconstructs the diffusion orientation distribution function (ODF), a spherical function that has its maxima agreeing with the underlying fiber populations. In this paper, we introduce the usage of the Diffusion Maps technique and show how it can be used to directly cluster set of fiber tracts, that could be obtained through a streamline tractography for instance, and how it can also help in segmenting fields of ODF images, obtained through a linear and regularized ODF estimation algorithm based on a spherical harmonics representation of the Q-Ball data. We first show the advantage of using Diffusion Maps clustering over classical methods such as N-Cuts and Laplacian Eigenmaps in both cases. In particular, our Diffusion Maps requires a smaller number of hypothesis from the input data, reduces the number of artifacts in fiber tract clustering and ODF image segmentation and automatically exhibits the number of clusters in both cases by using an adaptive scale-space parameter. We also show that our ODF Diffusion Maps clustering can reproduce published results using the diffusion tensor (DT) clustering with N-Cuts on simple synthetic images without crossings. On more complex data with crossings, we show that our ODF-based method succeeds to separate fiber bundles and crossing regions whereas the DT-based methods generate artifacts and exhibit wrong number of clusters. Finally, we illustrate the potential of our approach on a real brain dataset where we successfully segment well-known fiber bundles.

Unité de recherche INRIA Sophia Antipolis

2004, route des Lucioles, BP 93, 06902 Sophia Antipolis Cedex (France)

Téléphone : +33 4 92 38 77 77 — Télécopie : +33 4 92 38 77 65

Key-words: Spectral clustering, Diffusion Maps, Diffusion MRI, Diffusion Tensor Imaging, High Angular Resolution Diffusion Imaging, Q-Ball Imaging, Tractography

Spectral Clustering en IRM de diffusion pour Retrouver les Faisceaux de la Matière Blanche

Résumé : Regrouper en des ensembles cohérents les faisceaux de fibres qui constituent la matière blanche du cerveau est un problème difficile mais de fort intérêt dont la solution peut aider à resoudre toute une classe de problèmes en neuroimagerie dont par exemple la construction d'atlas et de cartes statistiques permettant d'améliorer notre compréhension de la structure du cervau humain. Ce problème se trouve compliqué encore plus par certaines configurations de fibres qui peuvent fusionner, se croiser ou diverger. Ce rapport se donne comme objectif d'aider à la résolution de ce problème en appliquant la technique dite des cartes de diffusion aux données d'IRM de Diffusion à haute résolution angulaire (HARDI) qui permettent de décrire les phénomènes de diffusion non-Gaussiens qui se produisent lorsque plusieurs faisceaux de fibres se croisent. En effet, contrairement au tenseur de diffusion classique (DTI), HARDI permet de décrire finement les croisements de faisceaux de fibres au sein de la matière blanche. Dans ce rapport, nous faisons usage d'une solution linéaire et régularisée pour estimer la function de distribution d'orientations des fibres (ODF) à partir d'imagerie HARDI telle que le Q-Ball et nous proposons de faire usage de la technique dite des cartes de diffusion pour d'une part regrouper directement les fibres obtenues par un algorithme de tractographie et d'autre part de segmenter les cartes d'ODF obtenues à partir de données d'IRM de Diffusion à haute résolution angulaire. On montre que notre méthode à base de cartes de diffusions permet de regrouper de façon cohérente un ensemble de fibres ou de segmenter correctement un champs d'ODF avec ou sans présence de croisements, dépassant ainsi en performance les approches classiques basées sur l'utilisation du tenseur de Diffusion qui ne peuvent traiter correctement les configurations singulières de type croisement. Les différentes potentialités de notre approche à base de cartes de Diffusion sont mises en valeur, comparées à celles de techniques plus classique (N-Cuts, Laplacien..) et finalement illustrées et évaluées sur différentes données synthétiques et réelles.

Mots-clés : Spectral clustering, Diffusion Maps, IRM de Diffusion, Imagerie par Tenseur de Diffusion (DTI), IRM de Diffusion à Résolution Angulaire (HARDI), Imagerie par Q-Ball (QBI), Tractographie

Contents

1 Introduction

Diffusion Magnetic Resonance Imaging (dMRI) is a unique non-invasive technique that allows to probe and quantify the diffusion of water molecules in the body. It was introduced in [LeBihan and Breton, 1985; LeBihan *et al.*, 1986; Merboldt *et al.*, 1985; Taylor and Bushell, 1985]. Diffusion MRI recovers the effective diffusion of water in tissues, thus providing unique biologically and clinically relevant information not available from other imaging modalities. This information can help characterize tissue micro-structure and its architectural organization [Basser and Pierpaoli, 1996] by modeling the local anisotropy of the diffusion process of water molecules.

Due to the capacity of dMRI for elucidating micro-structural features, the cerebral white matter fiber structure can be recovered using this imaging technique. In this work, we focus on two different methodologies developed in order to represent the diffusion of water within one voxel, Diffusion Tensor Imaging (DTI) and Q-Ball Imaging (QBI). Firstly DTI [Basser *et al.*, 1994b] assumes that the diffusion of water molecules follows a Gaussian distribution. While the Gaussian assumption is adequate for voxels in which there is only a single fiber orientation (or none), it breaks down for voxels in which there is more complicated internal structure with multiple crossing fibers. QBI [Tuch, 2004a] is a recent high angular resolution diffusion imaging (HARDI) technique that overcomes this limitation by reconstructing a diffusion orientation distribution function (ODF). The ODF is a spherical function that contains the angular information of the diffusion displacement probability of water molecules. Hence, it has its maxima agreeing with the underlying fiber distribution. The ODF reconstruction from QBI is attractive because it is model-free and has been recently shown possible with a regularized and analytical solution [Descoteaux *et al.*, 2007], which produces a robust and fast ODF reconstruction.

Once the diffusion information has been recovered within each voxel, it can be assembled through the volume in order to assess fiber connectivity in vivo. Two major class of techniques have been proposed in order to achieve this goal, streamline tractography [Mori *et al.*, 1999; Conturo *et al.*, 1999; Basser *et al.*, 2000], and probabilistic tractography [Koch *et al.*, 2002; Parker and Alexander, 2003; Behrens *et al.*, 2003b; Behrens *et al.*, 2003a; Lazar and Alexander, 2005]. The first one, streamline tractography, recovers fibers from a seed voxel by following the principal direction of the diffusion tensor or the diffusion ODF. The second approach, probabilistic tractography, traces the connectivity distribution of individual fibers. Given a seed voxel, it calculates the probability of that voxel being connected to every other voxel in the white matter.

It is known that efficient identification of white matter structures or segmentation of fiber tracts into bundles in dMRI data is an important problem in neuroimaging because it has many potential applications. For example, it could potentially provide important information on diseases that affect fiber tracts. Accurate reconstruction of the fiber tracts may provide new biomarkers in white matter pathologies and segmentation of these tracts could also improve our understanding of the functional role these tracts have and the cognitive consequences of their disruption. However, none of the existing methods that recover axonal fiber connectivity can directly be used in order segment well-known fiber bundles as the ones shown in figure 1 from [Gray, 1918]. In this work, we provide two techniques in order to recover white matter structures. The first technique, based on streamline tractography results, attempts to produce a

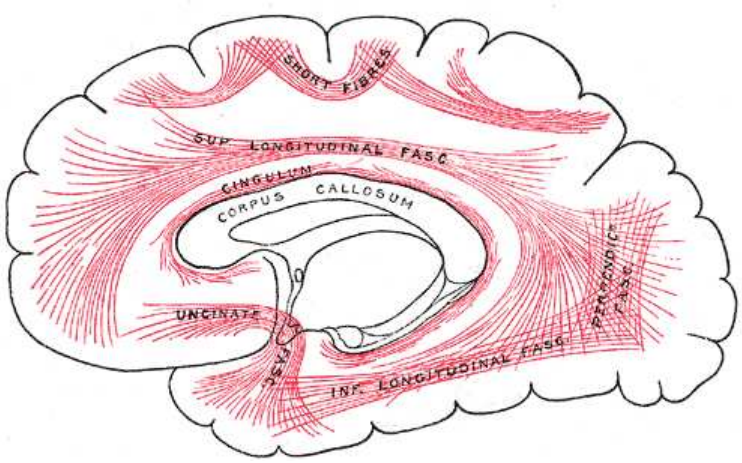

Figure 1: An illustration of classified white matter associative fibers. The ultimate goal of this work is to produce a classification of the data obtained from dMRI in such a way that the main fiber bundles are properly identified. From 20th U.S. edition of Gray's Anatomy of the Human Body (public domain)

clustering of the fiber tracts. The second approach, based on the segmentation of DT and Q-Ball images, attempts to perform a segmentation or a clustering of image regions into fiber bundles.

The goal of this work is to provide algorithms which will be able to identify fiber bundles through dMRI imaging. We do this through a manifold learning framework, spectral embedding and clustering, applicable to fiber tracts and ODFs. This provides means to compute statistics of these two types of data and ultimately lead to clustering and segmentation of fiber bundles. Spectral embedding and clustering methods have recently proved to be effective in manifold learning [Weiss, 1999; Brand, 2003; Saul and Roweis, 2003; Belkin and Niyogi, 2003] and image segmentation [Shi and Malik, 2000; Ziyan *et al.*, 2006]. However, these approaches require restrictive hypotheses that are difficult to meet in real applications. For instance, N-Cuts [Shi and Malik, 2000] and Laplacian Eigenmaps [Belkin and Niyogi, 2003], require data within each cluster to be uniformly sampled, which produces artifacts when this hypothesis is not met. Moreover the application of these approaches to image segmentation also assumes that the scale of each cluster is the same, thus using a single scale parameter for the whole dataset. In order to overcome these limitations, we propose to use Diffusion Maps [Coifman *et al.*, 2005] as spectral embedding method. This method looses the dependence on the sampling of the elements to cluster. Moreover, we propose to use an adaptive scale-space parameter in order to deal with scale differences across different clusters.

2 Diffusion MRI

In 1994, Basser et al. proposed the diffusion tensor model [Basser *et al.*, 1994c; Basser *et al.*, 1994a]. This model gave birth to DTI. It relies on the assumption that the diffusion of water molecules within each voxel can be modeled by a

Gaussian probability distribution. Hence, the probability of a water molecule starting at a given position, in our case the center of voxel, being displaced by a radial vector $\mathbf{r}$ in a time τ, is expressed as

$$P(\mathbf{r}) = \left(\frac{1}{(4\pi\tau)^3|\mathbf{D}|}\right)^{\frac{1}{2}} \exp\left(\frac{\mathbf{r}^\top \mathbf{D}^{-1}\mathbf{r}}{4\tau}\right). \quad (1)$$

The diffusion process within a voxel is then characterized with a rank-2 tensor, which is the symmetric 3×3 positive definite matrix $\mathbf{D}$. Using at least six different Diffusion Weighted (DW) images with different encoded gradient directions $\mathbf{g}$, the diffusion tensor can be reconstructed at each voxel in the volume. The resulting signal attenuation is given by the Stejskal-Tanner equation [Stejskal and Tanner, 1965],

$$S(\mathbf{g}) = S_0 \exp\left(-b\mathbf{g}^\top \mathbf{D}\mathbf{g}\right) \quad (2)$$

where b is the diffusion weighting factor depending on scanner parameters such as the length and strength of the diffusion gradient and time between diffusion gradient pulses and S_0 is the T2-weighted signal acquired without any diffusion gradients. Several techniques to do diffusion tensor estimation from DW images have been proposed [Westin *et al.*, 2002; Tschumperlé and Deriche, 2003; Wang *et al.*, 2003; Campbell, 2004; Lenglet *et al.*, 2006c; Arsigny *et al.*, 2006]

The DTI model lacks the capability of accurately modeling the diffusion of water particles where there are several fibers crossing the voxel in different directions. In order to overcome this limitation, QBI has been proposed by Tuch et al [Tuch, 2004b]. In this method, the angular information of the diffusion probability displacement of water molecules is reconstructed and is called the diffusion ODF. The ODF is defined as

$$\Psi(\mathbf{r}) = \frac{1}{Z}\int_0^\infty P'(\zeta\mathbf{r})d\zeta, \mathbf{r} \in S^2, \quad (3)$$

where S^2 is the unit-norm sphere, Z is a dimensionless normalization constant and $P'(\cdot)$ is the average diffusion displacement probability of water molecules.

The ODF $\Psi(\cdot)$ can be estimated at the cost of longer acquisition times than DTI by doing HARDI [Tuch *et al.*, 2002] acquisitions. The idea of HARDI is to sample the sphere in N discrete gradient directions (Fig. 2) and perform acquisitions on the N directions. Hence, the HARDI signal at each voxel is a discrete spherical function, $S(\mathbf{g})$, with no a priori assumption about the nature of the diffusion process within the voxel. [Tuch, 2004b] showed that an estimation of the ODF can be performed directly on the HARDI signal S by applying the Funk-Radon transform $\mathcal{G}[\cdot]$:

$$\Psi(\mathbf{r}) = \mathcal{G}[S](\mathbf{r}) = \int_{S^2} \delta\left(\mathbf{r}^\top \mathbf{s}\right) S(\mathbf{s})d\mathbf{s} \quad (4)$$

Intuitively, the Funk-Radon transform of a value at an arbitrarily defined "pole" of the signal on the sphere, is the integral of the spherical function S over the corresponding "equator" or great circle perpendicular to that "pole". This is illustrated in figure 3.

Several analytical solution of the Funk-Radon transform have recently been proposed [Descoteaux *et al.*, 2007; Anderson, 2005; Hess *et al.*, 2006]. These solutions are all based on the spherical harmonics representation of the HARDI signal, which gives a compact representation of the ODF.

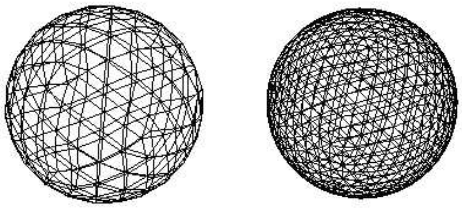

162 points 642 points

Figure 2: Discrete samplings of the sphere for different numbers of gradient directions corresponding to order 3 and order 4 tessellation of the sphere respectively.

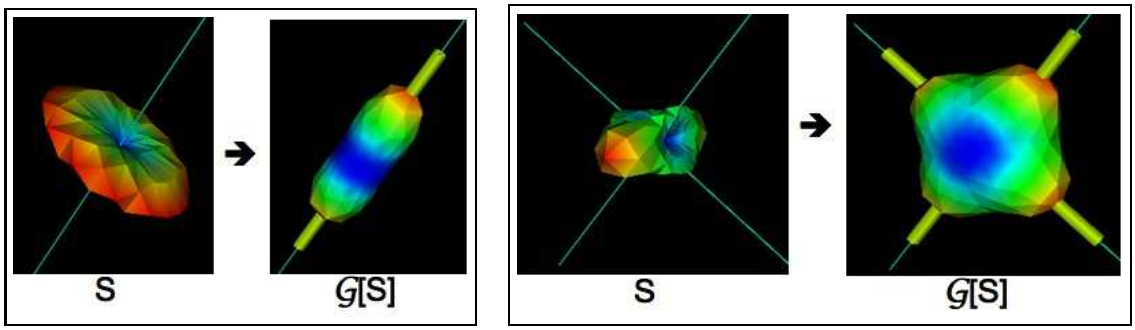

Figure 3: Funk-Radon Transform illustrated for the input diffusion attenuation signal S ($b = 1000$ s/mm^2) with 1 fiber (left) and two orthogonal fibers (right). The thin lines are the true underlying fiber directions and the thicker tubes are the detected maxima. One must imagine these functions as living on the surface of the sphere. Here, for visualization purposes, the radius of the respective spheres are scaled by the corresponding value on the surface. Blue to red colors represent low to high spherical values.

2.1 DTI estimation

DTI [Basser *et al.*, 1994c; Basser *et al.*, 1994a] reconstructs a rank-2 3×3 symmetric positive definite tensor, which represents the diffusion of a water molecule within a voxel and its called a diffusion tensor (DT). Given a T2, S_0, image and a gradient direction $\mathbf{g}_i$, the signal attenuation in that direction at the voxel at $\mathbf{x}$ of the image can be characterized with the equation

$$S_i(\mathbf{x}) = S_0(\mathbf{x}) \exp(-b\mathbf{g_i}^\top \mathbf{D}\mathbf{g_i}), \tag{5}$$

where $\mathbf{D}$ is the DT in one voxel of the image, thus what we are looking for. Applying the logarithm to both sides, of equation (5)

$$-\frac{1}{b} \ln\left(\frac{S_i(\mathbf{x})}{S_0(\mathbf{x})}\right) = \mathbf{g}_i^\top \mathbf{D}\mathbf{g}_i \tag{6}$$

Then taking several measurements S_i, following [Lenglet *et al.*, 2006c], a minimization algorithm that calculates the tensor by fitting it to the measurements can be obtained by calculating the tensor D which minimizes the energy:

$$E(S_0, \ldots, S_N) = \sum_i^N \psi\left(\frac{1}{b} \ln \frac{S_i}{S_0} + \mathbf{g}_i^\top \mathbf{D}\mathbf{g}_i\right), \tag{7}$$

where $\psi : \mathbb{R} \to \mathbb{R}$ is a functional that tries to reduce the effect of outliers. In what matters to the election of $\psi(\cdot)$ and other details of tensor estimation, we refer the interested reader to [Lenglet, 2006, section 6.1] and the references therein.

This energy, can be minimized within the space of symmetric positive definite matrices, following the gradient descent scheme [Lenglet, 2006, section 6.2]:

$$\mathbf{D}_{l+1} = \mathbf{D}_l^{\frac{1}{2}} \exp\left(-ds\mathbf{D}_l^{-\frac{1}{2}} \left(\sum_{i=1}^N \psi'(r_i(\mathbf{D}_l))\mathbf{D}_l\mathbf{g}_i(\mathbf{D}_l\mathbf{g}_i)^\top\right) \mathbf{D}_l^{-\frac{1}{2}}\right) \mathbf{D}_l^{\frac{1}{2}}, \tag{8}$$

where the residual r_i, of the approximation of D_l is

$$r_i(\mathbf{D}_l) = \frac{1}{b} + \ln\left(\frac{S_i}{S_0}\right) \mathbf{g}_i^\top D_l \mathbf{g}_i,$$

and the time step is ds.

Distances between diffusion tensors Once the DT is calculated, we want to capture similarities and dissimilarities between two DT. There have been seldom theoretical and practical justification of the disadvantages of using the matrix norm to quantify similarity between tensors [Lenglet *et al.*, 2006c; Arsigny *et al.*, 2006]. In order to solve this problems several metrics have been proposed [Lenglet *et al.*, 2006c; Arsigny *et al.*, 2006; Jonasson *et al.*, 2007]. In this work we follow [Lenglet *et al.*, 2006c], for a pair of tensors $\mathbf{D}$, $\mathbf{D}'$, the distance is defined as

$$d(\mathbf{D}, \mathbf{D}') = sqrt\frac{1}{2} \operatorname{trace}\left(\log^2\left(\mathbf{D}^{-\frac{1}{2}}\mathbf{D}'\mathbf{D}^{-\frac{1}{2}}\right)\right). \tag{9}$$

This distance has been successfully used to perform statistics in the tensor space, segmentation of DTI [Lenglet *et al.*, 2006c], DTI reconstruction [Castaño-Moraga *et al.*, 2007] and to provide brain connectivity metrics [Prados *et al.*, 2006].

2.2 Analytical ODF Estimation from QBI

As mentioned before, QBI [Tuch, 2004a] reconstructs the diffusion ODF directly from the HARDI measurements on a single sphere by the Funk-Radon transform (FRT). The ODF is intuitive because it has its maxima aligned with the underlying population of fibers. However, computing statistics on a large number of discrete ODF values on the sphere[1] is computationally heavy and infeasible to integrate into a segmentation algorithm of the whole brain. A more compact representation of the ODF is thus needed. [Descoteaux *et al.*, 2007; Anderson, 2005; Hess *et al.*, 2006] proposed a simple analytical spherical harmonic (SH) reconstruction of the ODF.

Letting Y_ℓ^m denote the SH of order ℓ and degree m ($m = -\ell, ..., \ell$), we define a modified SH basis that is real and symmetric. For $\ell = 0, 2, 4, ..., \ell_{\text{max}}$ and $m = -\ell, ..., 0, ..., \ell$, we define a single index j in terms of ℓ and m such that $j(\ell, m) = (\ell^2 + \ell + 2)/2 + m$. The modified basis is given by

$$Y_j = \begin{cases} \sqrt{2} \cdot \text{Re}(Y_\ell^m), & \text{if } m < 0 \\ Y_\ell^m, & \text{if } m = 0 \\ \sqrt{2} \cdot \text{Im}(Y_\ell^m), & \text{if } m > 0. \end{cases} \tag{10}$$

where $\text{Re}(Y_\ell^m)$ and $\text{Im}(Y_\ell^m)$ represent the real and imaginary parts of Y_ℓ^m respectively. The basis is designed to be symmetric, real and orthonormal because of the normalization factor $\sqrt{2}$. Moreover, note that there are exactly $L = (1/2)(\ell_{\text{max}} + 1)(\ell_{\text{max}} + 2)$ terms in the spherical harmonic series of order ℓ_{max}.

It is possible to obtain an analytical QBI solution ([Descoteaux *et al.*, 2007]) to obtain a final ODF Ψ with

$$\Psi(\theta, \phi) = \sum_{j=1}^{L} \underbrace{2\pi P_{\ell(j)}(0) c_j}_{f_j} Y_j(\theta, \phi), \tag{11}$$

where θ, ϕ obey physics convention ($\theta \in [0, \pi], \phi \in [0, 2\pi]$), $L = (\ell + 1)(\ell + 2)/2$ is the number of elements in the spherical harmonic basis, c_j are the SH coefficients describing the input HARDI signal, $P_{\ell(j)}$ is the Legendre polynomial of order $\ell(j)$[2] and f_j the coefficients describing the ODF Ψ. Here, we use the solution presented in [Descoteaux *et al.*, 2007] with a Laplace-Beltrami regularization of the SH coefficients c_j to obtain a more robust ODF estimation. The detailed implementation of the Laplace-Beltrami regularization and HARDI signal estimation is presented in [Descoteaux *et al.*, 2006a; Descoteaux *et al.*, 2007].

Distances between ODFs Once the ODF are computed, we want to capture similarities and dissimilarities between two ODFs, i.e two spherical functions $\Psi, \Psi' \in \mathbf{S}^2$ that can be represented by real SH vectors of length L, $f = \{f_1, ..., f_L\}$ and $f' = \{f'_1, ..., f'_L\} \in \mathbb{R}^L$, as shown in the previous section equation equation (11). Since the ODFs come from real physical diffusion measurements they are bounded and form an open subset of the space of real-valued $\mathcal{L}^2$ spherical

[1] Typically, the ODF is reconstructed on more than 200 discrete spherical values.

[2] $\ell(j)$ is the order associated with the j^{th} element of the SH basis, i.e. for $j = 1, 2, 3, 4, 5, 6, 7, ...$ $\ell(j) = 0, 2, 2, 2, 2, 2, 4, ...$

functions with an inner product $\langle , \rangle$ defined as

$$\begin{aligned} \langle \Psi, \Psi' \rangle &= \int_{\Omega} \Psi(\theta,\phi) \cdot \Psi(\theta,\phi)' d\Omega \\ &= \int_{\Omega} \left(\sum_{i=1}^{L} f_i Y_i(\theta,\phi) \sum_{j=1}^{L} f'_j Y_j(\theta,\phi) \right) d\Omega, \end{aligned} \tag{12}$$

where Ω denotes integration over the unit sphere. Because of the orthonormality of the spherical harmonic basis, $\int_{\Omega} Y_i(\theta,\phi) Y_j(\theta,\phi) d\Omega = \delta_{ij}$, the cross terms cancel and the expression is simply

$$\langle \Psi, \Psi' \rangle = \sum_{j=1}^{L} f_j \cdot f'_j. \tag{13}$$

Therefore, the induced $\mathcal{L}^2$ norm $||\Psi|| = \sqrt{\langle \Psi, \Psi' \rangle}$ giving us the distance metric between two ODFs is

$$||\Psi - \Psi'|| = \sqrt{\int_{\Omega} (\Psi(\theta,\phi) - \Psi'(\theta,\phi))^2 d\Omega} = \sqrt{\sum_{j=1}^{L} (f_j - f'_j)^2}. \tag{14}$$

The Euclidean distance was also used successfully for DTI segmentation in [Lenglet *et al.*, 2006a] even though more appropriate metrics exist such as the J-Divergence [Wang *et al.*, 2004; Lenglet *et al.*, 2006a] and Riemannian geodesic distances [Lenglet *et al.*, 2006c]. Similarly, one can think of choosing another metric to compare ODFs. For instance, since the ODF can be viewed as a probability distribution function (PDF) of fiber orientations, one can use the Kullback-Leibler distance between two PDFs, as done in [Tuch, 2004a]. However, in that case the problem quickly blows up computationally because one needs to use all N discrete HARDI data on the sphere instead of the L SH coefficients ($L << N$).

2.3 Tractography

DTI can now be used to investigate major nerve pathways in the brain [Basser *et al.*, 2002]. White matter fiber bundles of the human brain form a spatial pattern defined by the anatomical and functional architecture. Human brain atlases provide names for individual tracts and document that these patterns are comparable across subjects. Axonal connectivity measures, and thus tractography, are needed to understand functional coupling between cortical regions of the brain and is important for characterization of neuro-degenerative diseases, for surgical planning and for many other medical applications [Mori and van Zijl, 2002]. Currently, white matter fiber tractography is most commonly implemented using the principal diffusion direction of the DT data, in a streamline manner.

The classical streamline techniques [Mori and van Zijl, 2002; Conturo *et al.*, 1999; Basser *et al.*, 2000] represent axonal connectivity by a streamline fiber tract represented by a 3D curve which is estimated from dMR images. These techniques are based on the principal direction of the diffusion tensor, the eigenvector associated with the major eigenvalue. We denote $\mathbf{p}(s)$ as the curve parametrized by its arc-length. This curve can be computed as a 3D path adapting its tangent orientation locally according to vector field $\mathbf{v}(\cdot)$ defined by the eigenvector associated to the largest eigenvalue of each tensor. Hence, for a given starting point $\mathbf{p}_0$, we solve $\mathbf{p}(t) = \mathbf{p}_0 + \int_0^t \mathbf{v}(\mathbf{p}(s)) ds$. The integration is

typically performed numerically with Euler or Runge-Kutta schemes of order 2 or 4. In the Euler case, we have the discrete evolution equation

$$\mathbf{p}_{n+1} = \mathbf{p}_n + \mathbf{v}(\mathbf{p}_n)\Delta s, \tag{15}$$

where Δs is a small enough step size to obtain subvoxel precision. A continuous linear, cubic, spline or geodesic [Lenglet *et al.*, 2006b] interpolation of the vector field can be done at each step for the subvoxel points. A good review is found in [Mori and van Zijl, 2002] and more recently in [Campbell *et al.*, 2005; Hagmann *et al.*, 2006]. When working with Q-Ball images, the $\mathbf{v}(\cdot)$ can also be obtained from the maxima of the ODF function [Deriche and Descoteaux, 2007].

For seed point $\mathbf{p}_0$, for a given anisotropy measure *Am* that can be the fractional anisotropy (FA) [Basser and Pierpaoli, 1996] or any other anisotropy measure, for anisotropy threshold t_{aniso}, for curvature threshold t_θ.

Data: Given $\mathbf{p}_0$, *Am*, t_{aniso}, t_θ

1 **Set** $n = 0$;

2 Update curve according to Eq. 15 obtaining $\mathbf{p}_{n+1}$;

3 **If** $Am(\mathbf{p}_{n+1}) < t_{aniso}$ **then** STOP;

4 **If** $\dfrac{\mathbf{v}(\mathbf{p}_{n+1}) \cdot \mathbf{v}(\mathbf{p}_n)}{||\mathbf{v}(\mathbf{p}_{n+1})||||\mathbf{v}(\mathbf{p_n})||} > t_\theta$ **then** STOP ;

5 **Set** $n = n+1$ and **goto** 2;

Finally the result for one seed point is a streamline

$$F = \{\mathbf{p}_0, \ldots, \mathbf{p}_n\}.$$

Distances between fiber tracts Once the streamline fiber tracts have been calculated we want to be able to measure similarities between them. Several metrics have been proposed in order to perform this [Brun *et al.*, 2003; Corouge *et al.*, 2005; O'Donnell and Westin, 2006]. In this work we follow the approach of [O'Donnell and Westin, 2006] due that it takes in account the whole geometry of the fiber, as a difference to [Brun *et al.*, 2003] and that it is simple and more efficient to calculate than the one proposed in [Corouge *et al.*, 2005]. Given two fiber tracts F and F', an asymmetric distance from F to F' is calculated as,

$$asymmetricDistance(F,F') = \sqrt{\frac{\sum_{\mathbf{p}\in F} \min_{\mathbf{p}'\in F'}(\|\mathbf{p}-\mathbf{p}'\|^2)}{|F|}}, \tag{16}$$

and to make this symmetrical

$$d(F,F') = \frac{asymmetricDistance(F,F') + asymmetricDistance(F',F)}{2}. \tag{17}$$

This distance has already been used to perform fiber tract clustering in [O'Donnell and Westin, 2006], however the clustering algorithm is susceptible to artifacts coming from the distribution of the fiber tracts.

3 Spectral embedding and clustering

The main goal of this work is to produce techniques able to extract fiber tract bundles from dMRI images. One of the main problems to confront in this matter is the high dimensionality of the data to be treated. In this work we are dealing with two approaches to represent the axonal connectivity using dMRI:

Fiber tracts: Small bundles of axons can be extracted from dMRI using streamline tractography techniques (section 2.3). Each small bundle of axons, a *fiber tract* F, can be represented as a sequence of points

$$F = \{\mathbf{p}_0, \ldots, \mathbf{p}_N\}, \forall i : \mathbf{p}_i \in \mathbb{R}^3$$

White matter structures can then be recovered by clustering fiber tracts together. Nevertheless each fiber tract can have a length between tenths and thousands of points making the procedure of dealing with this structures all together computationally expensive. Moreover in order to produce a clustering, a measurement of similarity across fiber tracts, which are of highly variable length and shape, is needed.

dMRI Images Q-Ball images:] The diffusion probability function within each voxel of a dMRI can be modeled by a Diffusion Tensor (DT) and also by a Q-Ball, section 2. As seen in section 2.2, each diffusion tensor $\mathbf{D}$, can be represented by a matrix

$$\mathbf{D} = \begin{pmatrix} \mathbf{D}_{xx} & \mathbf{D}_{xy} & \mathbf{D}_{xz} \\ \mathbf{D}_{xy} & \mathbf{D}_{yy} & \mathbf{D}_{yz} \\ \mathbf{D}_{xz} & \mathbf{D}_{yz} & \mathbf{D}_{zz} \end{pmatrix}. \tag{18}$$

On the other hand, each Q-Ball Ψ can be represented as a set of real coefficients,

$$\Psi = \{f_0, \ldots, f_L\}, \forall i : f_i \in \mathbb{R}.$$

In both cases the elements representing the diffusion profile, $\mathbf{D}$ and Ψ, are located at a voxel in the image. Hence, each element in a dMRI image can be characterized by a spatial position $\mathbf{p} \in \mathbb{R}^3$ and a set of real coefficients. In the DT case the coefficients are 6 while in the Q-Ball, following [Frank, 2002] and [Descoteaux *et al.*, 2007], at least 15. This means at least $3+6=9$ dimensions per element. In order to recover white matter structures, a clustering of these elements must be produced taking in account two different characteristics of the element, spatial position $\mathbf{p}$ and diffusion profile, either $\mathbf{D}$ or Ψ.

In both cases, the problem of recovering white matter structures, can be reduced to an element clustering problem. Moreover, in both cases the elements to be clustered exhibit two characteristics.

In the first place, high extrinsic dimensionality of each element. In the fiber tract case, each element exhibits a variable dimensionality between tenths and thousands of dimensions, and in the dMRI images case, although all the elements in one image have the same dimensionality, each element has at least 9 dimensions.

Secondly, the intrinsic dimensionality of the data is smaller than the extrinsic one. This means that, for instance in the Q-Ball case, although each element can be expressed as an array of 18 real numbers, not every array of 18 real

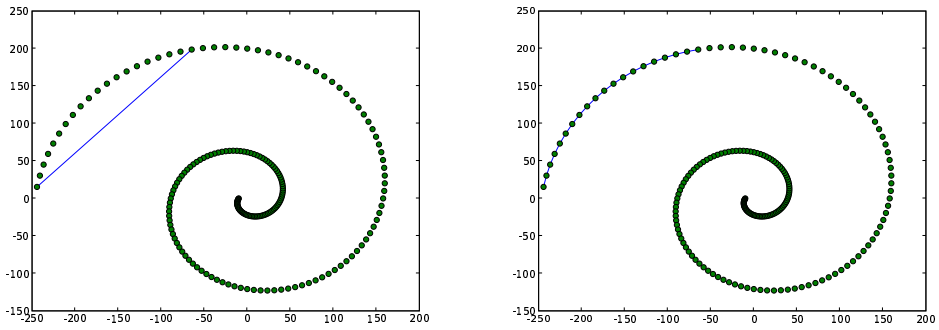

(a) Blue curve depicting extrinsic distance

(b) Blue curve depicting intrinsic distance

Figure 4: Intrinsic versus extrinsic geometrical interpretation. A spiral dataset, whose intrinsic dimensionality is one is shown embedded in an extrinsic two-dimensional space. The blue curves depict distance in the extrinsic 4(a) and intrinsic 4(b) geometries.

numbers represents a valid element. In the fiber tract case, not every sequence of three-dimensional points represents a valid fiber tract in the white matter of the analyzed brain. In this work we take the hypothesis, as in [Tenenbaum *et al.*, 2000; Roweis and Saul, 2000], that the data actually resides in a manifold whose dimension is lower than the actual space where the elements *live*. More formally, noting the space where the elements live S (e.g. in the Q-Ball case $S = \mathbb{R}^{18}$), the elements of our set X by the smooth function,

$$I : O \rightarrow \mathcal{M} \subset S,$$

where O is some parametrization of the set and X is a discrete sampling of the continuous differentiable manifold $\mathcal{M}$.

In order to illustrate the difference between extrinsic and intrinsic dimensionality and the associated extrinsic and intrinsic metrics, we show in figure 4 a spiral data-set. In this case $O = [\pi, 4\pi]$, $I(\theta) = \theta^2(\cos(\theta), \sin(\theta))$ and $\mathcal{M} = I(O) \subset \mathbb{R}^2$. The extrinsic space S is $\mathbb{R}^2$ where the distance between two elements of X, $I(\theta)$ and $I(\theta')$, is the Euclidean distance in $\mathbb{R}^2$, $d_{ex}(I(\theta), I(\theta')) = \|I(\theta) - I(\theta')\|$, shown in figure 4(a). On the other hand, the intrinsic geometry, more appropriate to quantify similarity between two points of our spiral, is $I(O)$. Within this geometry, the intrinsic distance between two points $I(\theta)$ and $I(\theta')$ is the length of the arc joining the two points, $d_{in}(I(\theta), I(\theta')) = \int_{\theta}^{\theta'} \|I'(s)\| ds$, shown in figure 4(b).

These characteristics lead to the following algorithm sketch which formulates the problem of recovering white matter fiber structures as a clustering problem,

Data: Given a set X of elements x

1 *Learn* the structure of the manifold $\mathcal{M} \subset S$;

2 Find a metric m associated to the intrinsic geometry of the manifold $\mathcal{M}$;

3 Use the metric m to calculate the similarity between the elements of X and produce a clustering $C = \{C_0, \ldots, C_K\}$, where $\bigcup_i C_i = X$;

.

To implement the presented algorithm we will resort to spectral manifold learning and clustering. In recent years, spectral manifold learning and clustering techniques [Belkin and Niyogi, 2003; Roweis and Saul, 2000; Shi and Malik, 2000; Tenenbaum *et al.*, 2000; Weiss, 1999], have become one of the most popular modern clustering family of methods. They are simple to implement, they can be solved efficiently by standard linear algebra software and very often they outperform traditional manifold learning and clustering algorithms such as the classical PCA (Principal Component Analysis) [Jolliffe, 1986] and k-means [Jain *et al.*, 1999] algorithms.

Spectral embedding reduces the problem of manifold learning to an eigenvalue decomposition (EVD) problem and spectral clustering reduces the clustering problem to a graph partitioning problem. Each element $x \in X$ to be clustered is represented as a node in a graph and the edges joining each pair of nodes are weighted by measure of the affinity between the elements. This affinity measure lies between 0 and 1, 0 being the less affine case. A spectral decomposition of this graph is taken by calculating the eigenvalue decomposition of the graph Laplacian [Chung, 1997]. Then a low-dimensional manifold embedding is inferred from this decomposition. This family of techniques produces a mapping of each element of $x \in X$ to a vector of real valued components such that the L_2 norm can be used as an approximation of the metric m associated to the manifold $\mathcal{M}$. Due to this we say that the embedding manifold has an Euclidean representation. Finally, the clustering is performed in the inferred Euclidean manifold.

All the above techniques rely on three hypotheses:

1. Preservation of the distance relationship: after a distance is defined between elements, the learned manifold should preserve the distance relation.

2. Uniform sampling of the elements: the density of the extracted elements changes if and only if these elements belong to anatomically different bundles.

3. Convexity of $\mathcal{M}$: Given two elements from X, almost all of the intermediate elements obtained by the interpolation that can be inferred from the metric used to build the affinity matrix are in the data set.

It is not easy to guarantee that the data to be embedded and clustered will adhere to these hypotheses. Donoho et al., in [Donoho and Grimes, 2005], analyze when a spectral embedding algorithm is able to recover the true parametrization of a set of images.

With respect to tractographies, the process from the DW images to the streamline tractography is composed from several steps like estimation, seeding the tracking process itself, every process has its conditions and variable dependence which makes hard to guarantee any of the hypothesis. On the other hand, as DT and Q-Ball images represent

the discretization of a continuous space, hypotheses 1 and 3 are plausible for the Q-Ball case, even though there is no indication that within a fiber bundle the distribution of the Q-Balls Ψ is uniformly sampled.

Moreover, in [Lafon, 2004] it is shown that different sampling frequencies within one cluster leads the N-Cuts [Shi and Malik, 2000] and Laplacian Eigenmaps [Belkin and Niyogi, 2003] methods to subdivide the cluster in several parts. In order to overcome this limitation and to be resilient to sampling frequency differences within a cluster, we use the Diffusion Maps [Coifman *et al.*, 2005] spectral embedding technique. We now describe the three steps involved in the Diffusion Maps manifold learning and clustering algorithm.

Step 1: Computing the affinity matrix Letting X represent the set of all elements $x \in \mathbb{R}^N$, to cluster, the main idea is to look for a coordinated representation of the elements of X that captures the intrinsic geometry of the set, oftently reducing the dimensionality of the elements. With this in mind, a fairly good way of representing any set of elements with an affinity function $a : X \times X \to \mathbb{R}_{>0}$, is a weighted graph, $G(X,E,w(\cdot))$ where the weight of the edge between two vertices represents the affinity of the elements connected by this edge. More formally, for an edge, $(x_i,x_j) \in E$, the weight of the edge is $w(v) = a(x_i,x_j)$. Hence, each element of the adjacency matrix of G or conversely the affinity matrix of $(X,a(\cdot))$ is

$$A_{ij} = a(x_i,x_j),$$

where $A \in \mathbb{R}^{|X|\times|X|}$, $|X|$ being the size of X. Then, the weighted graph $G(X,E,w(\cdot))$ can be also noted as $G(X,A)$.

Usually a distance function $d(\cdot)$ instead of an affinity function is given. The distances can be easily converted into affinities by applying a kernel to the distance function:

$$a(x_i,x_j) = e^{-\frac{d(x_i,x_j)^2}{\sigma_{ij}^2}}, \tag{19}$$

where σ is an adaptative scale space parameter and may depend on the elements x_i and x_j. In this work, an adaptative scale-space parameter is considered following [Zelnik-Manor and Perona, 2004]. A "neighbor-number" k is given as parameter to the algorithm and then $\sigma_{ij}^2 = d(x_i,x_{i_k})d(x_j,x_{j_k})$ where x_{i_k} is the k-th closest neighbor according to the distance function $d(\cdot,\cdot)$ of element x_i. This choice of a scaling parameter for each point allows self-tuning of the point-to-point distances according to the local statistics of the neighborhoods surrounding points i and j.

To illustrate this process we reintroduce the spiral dataset shown in figure 4. The function to generate the dataset is $I(\theta) = \theta^2(\cos(\theta),\sin(\theta))$. The sampling is uniformly taken over the parameter θ, $O = \left\{\pi, \pi+\frac{1}{50}, \pi+\frac{2}{50}, \ldots, 4\pi\right\}$. The dataset $X = I(O)$, and the squared distance matrix where $d_{ij} = \|I(\theta_i) - I(\theta_j)\|^2$ are shown in figure 5. In this figure it can be seen that although O is uniformly distributed, $X = I(O)$ is not. This is shown in figure 5(a) in the concentration difference between the two edges of the spiral, and in the distribution of the distances in figure 5(b). In this matrix the higher rows and columns exhibit higher values in general due to the distribution of distances at the edge of the spiral which is further away from the center. In the edge which is closer to the center the distances are smaller.

We can now illustrate two affinity matrices, one where the σ parameter is fixed for the whole dataset and one where it is adaptative. This is shown in figure 6. It can be noticed that in the non-adaptative affinity matrix, figure 6(a), the

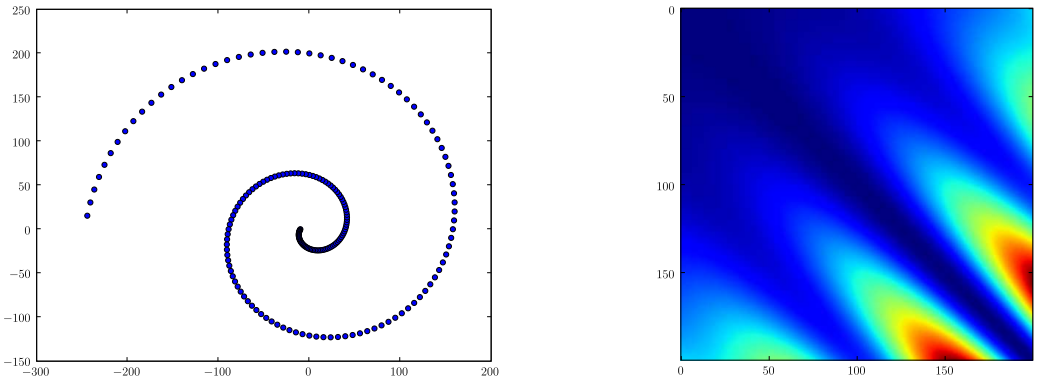

(a) spiral dataset (b) squared distance matrix

Figure 5: Spiral dataset and its squared distance matrix. The distribution of the points on the spiral is not uniform, this can be noted in the density difference in the edges of the spiral, figure 5(a). It can be also noticed in the dominant intensities in the upper left and lower right corners of the squared distance matrix, figure 5(b), the color scale is blue for low values and red for high values.

concentration of the affinities changes along the diagonal, making the algorithm sensitive to scale differences. In the adaptative affinity matrix, figure 6(b), this change is not present due to the self adjustment of the affinities to the local scale of each element.

Step 2: Performing the embedding The algorithm must embed the elements of X into a n-dimensional Euclidean space $\mathbf{y}(X)$, where $n << |X|$ and where $X \subset \mathbb{R}^N$, $n << N$. This is achieved by performing spectral decomposition of the Laplacian of the graph whose connectivity matrix is A. More formally the algorithm should find mapping function $\mathbf{y} : X \rightarrow R^n$, $n \ll |X|$ that minimizes the energy

$$E(X,A) = \text{trace}\left(\sum_{i,j=1}^{|X|} (\mathbf{y}_i - \mathbf{y}_j)^2 A_{ij}\right), \mathbf{y}_i \in \mathbb{R}^n, \tag{20}$$

where $\mathbf{y}_i = \mathbf{y}(x_i), x_i \in X$. This produces an embedding compliant with hypothesis 1.

Following [Shi and Malik, 2000; Belkin and Niyogi, 2003], finding the mapping $\mathbf{y} : X \rightarrow \mathbb{R}^n$ is equivalent to find the matrix

$$Y = \begin{pmatrix} \mathbf{y}_0 \\ \vdots \\ \mathbf{y}_{|X|-1} \end{pmatrix} \in \mathbb{R}^{|X| \times n}$$

which minimizes

$$E(X,A) = \text{trace}(Y^\top \Delta(A) Y). \tag{21}$$

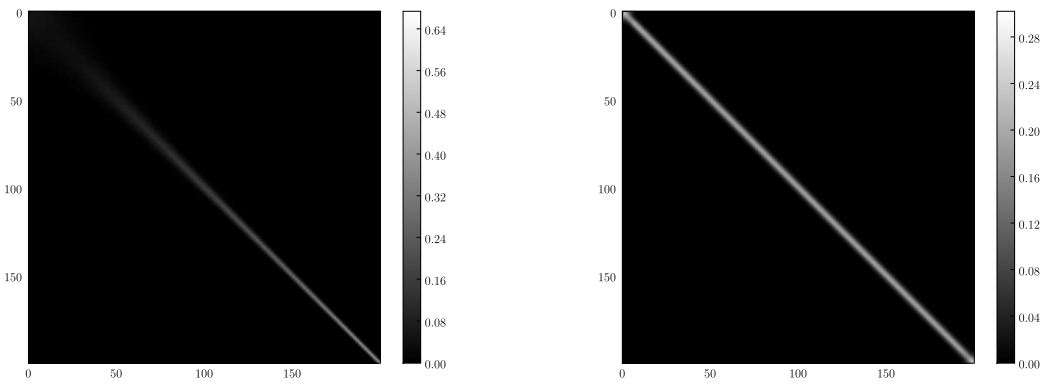

(a) non-adaptative affinity matrix

(b) adaptative affinity matrix

Figure 6: Affinity matrices for the spiral dataset. It can be noticed that in the non-adaptative affinity matrix, figure 6(a), the concentration of the affinities changes along the diagonal, making the algorithm sensitive to scale differences. In the adaptative affinity matrix, figure 6(b), this change is not present due to the self adjustment of the affinities to the local scale of each element.

The matrix $\Delta(A)$ is the Laplacian of the graph induced by the connectivity matrix A as defined in [Chung, 1997],

$$\Delta(A) = D(A) - A \in \mathbb{R}^{|X|\times|X|}, \tag{22}$$

with,

$$\{D(A)\}_{ij} = \begin{cases} \sum_k A_{ik} & i = j \\ 0 & i \neq j \end{cases}.$$

The minimization of Y is subject to two conditions,

$$\mathbf{y}_i^\top D(A)\mathbf{1} = 0$$

to avoid arbitrary translations, and

$$Y^\top D(A) Y = \mathbf{I} \in \mathbb{R}^{n\times n}$$

to obtain an orthogonal n dimensional base.

Providing that the graph that induced matrix A is fully connected [Chung, 1997, Lemma 1.7], then the matrix $Y \in \mathbb{R}^{|X|\times n}$ which gives an embedding and minimizes the energy (20) is

$$Y = \left(\lambda_1 \mathbf{v}^1 \cdots \lambda_n \mathbf{v}^n\right) \in \mathbb{R}^{n\times|X|},$$

where

$$0 = \lambda_0 < \lambda_1 \leq \cdots \leq \lambda_{|X|-1}$$

are the eigenvalues of $\Delta(A)$ and

$$V = \left(\mathbf{v}^0 \dots \mathbf{v}^{|X|-1}\right) \in \mathbb{R}^{|X|\times|X|}$$

the eigenvectors.

The eigenvector $\mathbf{v}_0$ is discarded due that its constant ($\forall i : \mathbf{v}_i^0 = a \in \mathbb{R}$), hence meaningless in order to calculate an embedding because it maps every element in X to the same point $a\mathbf{1}$.

Finally, the value of the energy E is $\sum_{i=1}^{n} \lambda_i$. Which means that the mapping for the element x_i, is defined as

$$\mathbf{y}_i = \mathbf{y}(x_i) = \left(\lambda_1 \mathbf{v}_i^1, \lambda_2 \mathbf{v}_i^2, \cdots, \lambda_n \mathbf{v}_i^n\right).$$

Diffusion maps In order to overcome the necessity of hypothesis 2, we pre-normalize the affinity matrix, as done in the diffusion maps technique [Coifman *et al.*, 2005]. This is done by normalizing the weight of each edge of the graph, A_{ij}, by the probability density of both elements relating through the edge,

$$W_{ij} = \frac{A_{ij}}{p(i)p(j)}, \tag{23}$$

where $p(\cdot)$, the probability density function of the elements in X, is not known but can be approximated, up to a multiplication factor, by,

$$p(i) = \sum_{k=0}^{|X|} A_{ik} = \sum_{k=0}^{|X|} A_{ki}.$$

The reasoning behind this solution is explained in appendix A

Due to the necessity of having a uniform behavior of the clustering algorithm without minding the scale of the affinity measure taken, a doubly stochastic matrix normalization is performed

$$\tilde{W} = \left(D(W)^{-1/2}\right) W \left(D(W)^{-1/2}\right) \in \mathbb{R}^{|X|\times|X|},$$

As the sum of each row of $\tilde{W}$ is 1, equation (22) can be rewritten as,

$$\Delta(\tilde{W}) = D(\tilde{W}) - \tilde{W} = I - \tilde{W}.$$

Then, instead of calculating the EVD of $\Delta(\tilde{W})$, the Singular Value Decomposition (SVD) of $\tilde{W}$ can be taken,

$$\tilde{W} = USU^\top \in \mathbb{R}^{|X|\times|X|}.$$

Finally, the Euclidean coordinates $\mathbf{y}_i$ of an element $x_i \in X$ in the n-dimensional embedding manifold are, ordering the eigenvalues in decreasing sense,

$$\mathbf{y}(x_i) = \mathbf{y}_i = \frac{1}{\mathbf{u}_i^0}\left(\mu_1 \mathbf{u}_i^1, \dots, \mu_n \mathbf{u}_i^n\right)^T, x_i \in X$$

where

$$U = \left(\mathbf{u}^0 \cdots \mathbf{u}^{|X|-1}\right) \in \mathbb{R}^{|X|\times|X|}$$

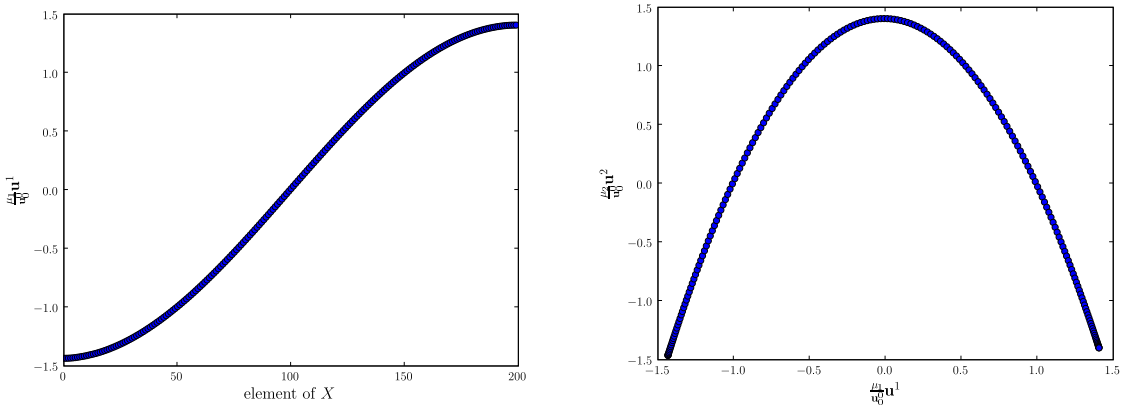

(a) one-dimensional embedding

(b) two-dimensional embedding

Figure 7: Embedding of the spiral dataset. The one and two-dimensional embeddings of the spiral dataset shown in figure 4. The first one, figure 7(a), using the ordered elements of X against the first non-constant normalized eigenvector $\frac{\mu_1}{\mathbf{u}_0^0}\mathbf{u}^1$. The second one, figure 7(b), using the two first non-constant normalized eigenvectors $\frac{\mu_1}{\mathbf{u}_0^0}\mathbf{u}^1$, $\frac{\mu_2}{\mathbf{u}_0^0}\mathbf{u}^2$.

is the eigenvector column matrix and the corresponding eigenvalues are, $1 = \mu_0 \geq \mu_1 \geq \cdots \geq \mu_{|X|-1} \geq 0$. The first eigenvector $\mathbf{u}_0$, is not taken into account as a component in the embedding because it is constant and hence meaningless, as shown in [Belkin and Niyogi, 2003; Chung, 1997; Coifman *et al.*, 2005], but is used as a scale factor. In order to illustrate the process, the one and two-dimensional embedding of the dataset shown in figure 4. This embeddings, shown in figure 7, are done using the diffusion maps technique with an adaptative affinity matrix. The coordinates for each element in the one-dimensional embedding, figure 7(a), are given by $(i, \frac{\mu_1}{\mathbf{u}_0^0}\mathbf{u}_i^1)$. In the two-dimensional embedding, figure 7(b), the coordinates are $\frac{1}{\mathbf{u}_0^0}(\mu_1\mathbf{u}_i^1, \mu_2\mathbf{u}_i^2)$, where i is the element number in X.

Step 3: Clustering Once the embedding has been performed, several techniques have been proposed for the clustering step. [Shi and Malik, 2000; Belkin and Niyogi, 2003; Lafon and Lee, 2006]

The first step in this process is to determine the number of clusters, this can be done in two ways. The first, as in [Nadler *et al.*, 2006], by choosing the number of clusters according to a big change in the curvature of the eigenvalue plot, or "elbow". For instance, if the slope of the eigenvalue plot changes noticeably at eigenvector λ_i, the number of clusters should be $i+1$. The second way is re-ordering the affinity matrix rows and columns following the second eigenvector, as proved in [Fiedler, 1975], which shows the block structure of the matrix as squared blocks along the matrix diagonal. Then, the number of clusters is the number of blocks. The recommended number of dimensions for the embedding is the same as the number of clusters. Finally, the clustering is performed by running a k-means clustering algorithm on the space spanned by $\mathbf{y}(X)$. A formal justification for this approach can be found in [Belkin and Niyogi, 2003; Lafon and Lee, 2006].

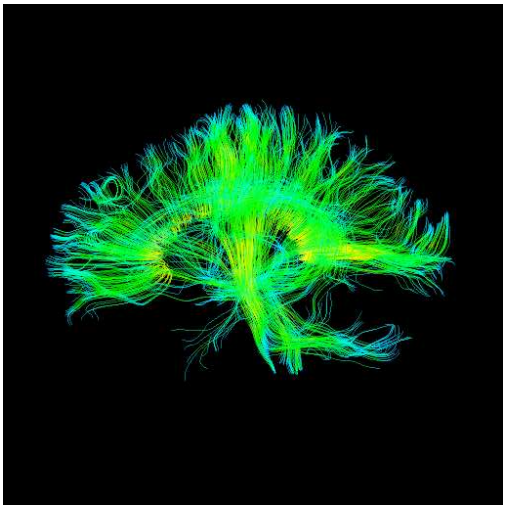

Figure 8: Streamline tractography example. The fibers are colored according to the anisotropy of the water diffusion in each segment. The cluttering of the fibers makes difficult to get insight of the data.

4 Fiber bundle identification through streamline tractography clustering

Tractography applied to the DT or ODF fields from diffusion weighted imaging, as seen in section 2, results in sets of streamlines which can be associated with major fiber tracts. If fibers are reconstructed and visualized individually through the complete white matter, the display gets easily cluttered making it difficult to get insight in the data, as it is shown in figure 8. In order to generate atlases, perform clear visualizations and compute statistics across subjects, various manifold learning and clustering techniques based on spectral embeddings and graph laplacians have been proposed [Brun *et al.*, 2004; Maddah *et al.*, 2005; O'Donnell and Westin, 2006]. Nevertheless the lack of ground truth images bounds the quality assessment of these processes to visual validation performed by experts which is far from being exhaustive. In this section we apply spectral embedding and clustering techniques to sets of streamlines or fiber tracts in order to associate the streamlines with major fiber bundles. Moreover, we show that some of the hypothesis of the spectral embedding techniques normally used are not met, thus having a high probability of generating artifacts in the embedding space and in the clustering. In this section we apply the spectral manifold learning and clustering techniques from section 3 to the tractography results obtained with the technique shown in section 2.3. We introduce the Diffusion Maps technique which relaxes the hypothesis of uniform sampling, thus reducing the probability of generating artifacts in the embedding.

In order to show the consequences of the drawbacks of the already used spectral clustering algorithms in fiber tract clustering [Brun *et al.*, 2004; Maddah *et al.*, 2005; O'Donnell and Westin, 2006], these algorithms were applied, in the first place to synthetic data. Then the same drawbacks are shown in a small real data set. Finally our algorithm is applied to set of streamline tracts emanating from the cortex showing clustering of the tracts into anatomically meaning fiber bundles.

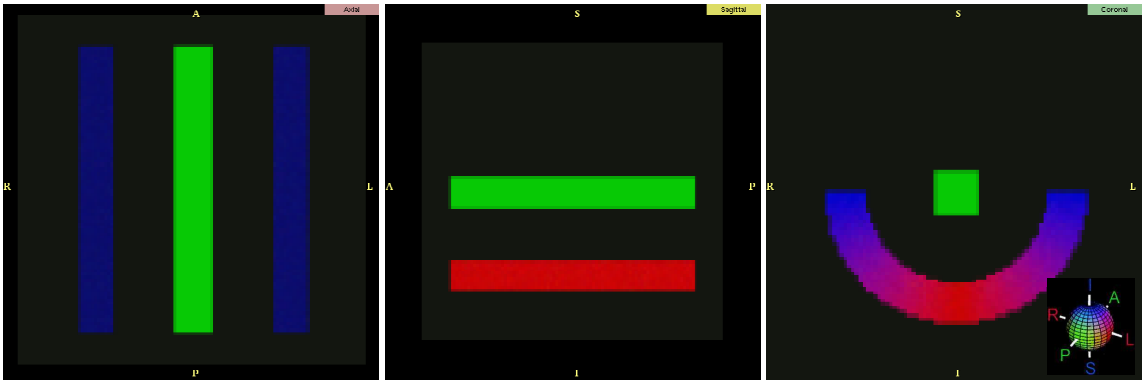

(a) axial (b) sagittal (c) coronal

Figure 9: Synthetic tensor data simulating a simplified fiber bundle set composed of the corpus callosum and the cingulum, the coloring is the usual color-by-orientation system.

4.1 Diffusion Weighted Data Generation and Acquisitions

4.1.1 Synthetic data

We generate synthetic HARDI data using the multi-tensor model which is simple and leads to an analytical expression of the ODF [Descoteaux *et al.*, 2006a; Tuch, 2004a]. For a given b-factor and noise level, we generate the diffusion-weighted signal

$$S(\mathbf{u}_i) = \sum_{k=1}^{n} \frac{1}{n} \exp(-b\mathbf{u}_i^{\mathrm{T}} \mathbf{D}_{\mathbf{k}}(\theta)\mathbf{u}_i) + noise \tag{24}$$

where $\mathbf{u}_i$ is the i^{th} gradient direction on the sphere, n is the number of fibers and $1/n$ is the volume fraction of the of each fiber. In practice, we use $N = 12$ from a 3^{rd} order tessellation of the icosahedron, $b = 700$ s/mm^2 and $n = 1$ or 2. $\mathbf{D}_{\mathbf{k}}(\theta)$ is the diffusion tensor with standard eigenvalues $[3, 3, 1.7]$x10^{-2} mm^2/s oriented in direction θ, which agree with reported physiological values [Pierpaoli *et al.*, 1996]. Finally, we add complex Gaussian noise with standard deviation of $1/35$, producing a signal with signal to noise ratio (SNR) of 35. The synthetic data depicts a simplification of the tracts of the corpus callosum(CC) and the cingulum(CG) fiber bundles. Diffusion weighted images (DWI) of 100^3 voxels, then the DT image is estimated using the technique introduced in section 2.1. The resulting Diffusion Tensor Image,

Uniform sampled clusters Given this synthetic dataset, two tract bundles were tracked, as explained in section 2.3, by seeding in two regions of interest, as shown in figure 10, the cyan one corresponding to the synthetic CC and the magenta one corresponding to the CG. The results of these tractographies are shown in figure 10, where 395 tracts have been found for the CC and 30 for the CG, making a total number of 425 tracts.

Following [O'Donnell, 2006], we used the distance introduced in section 2.3, equation (17). Then the obtained distance d is composed with a kernel $e^{-\left(\frac{d}{\sigma}\right)^2}$, taking $\sigma = 2$, in order to compute the affinity matrix. The affinity

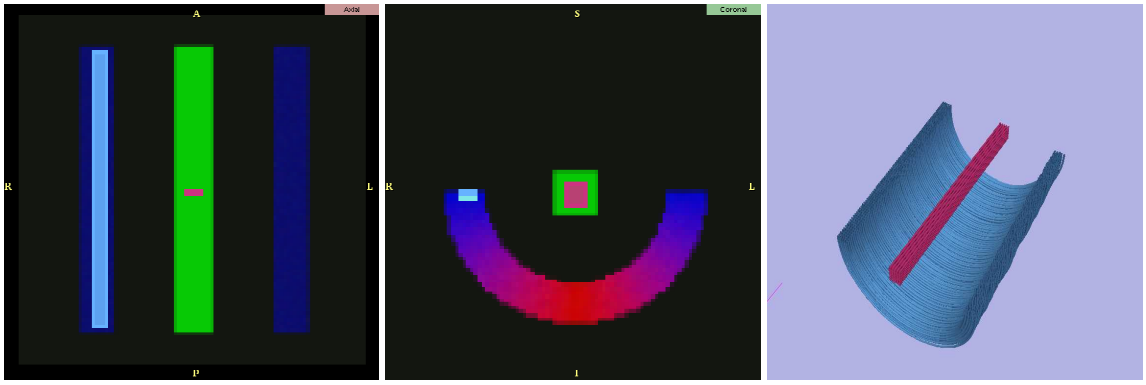

(a) axial (b) coronal (c) tractography

Figure 10: Regions of interest used to seed the tractographies shown in axial, (a), and coronal, (b), views, the cyan one corresponding to the synthetic CC and the magenta one corresponding to the CG. The resulting tract bundles manually colored according to the regions (c).

matrix, where the two bundles are clearly distinguished is shown in figure 11(a), the bigger 10 eigenvalues, of the normalized affinity matrix are shown in figure 11(b) and the 2-dimensional normalized embedding in figure 11(c). It can be noticed by observing the eigenvalues plot, that the clusters to be found is 2 and that they are clearly separable in this embedding.

Whereas in figure 12, the results with a $\sigma = 10$ can be seen, in this case, the k-means method will not succeed in clustering the bundles, showing that the success of the clustering final step based on the k-means algorithm, as recommended in [Shi and Malik, 2000; Belkin and Niyogi, 2003; Lafon and Lee, 2006], is highly sensitive to the adopted parameters.

Non-uniform sampled clusters In order to exhibit the sensitivity of the Normalized Cuts based algorithm [Brun *et al.*, 2004; Maddah *et al.*, 2005; O'Donnell and Westin, 2006] to hypothesis 2, a non-uniform seeding of the synthetic CC fiber bundle was performed as shown in figure 13 where 269 tracts conform the CC and 40 the CG.

The results of the embedding and clustering procedure are shown in figure 14. Observing the eigenvalues plot, it can be noticed that the number of clusters to be found is between 3 and 4; with respect to the embedding, it shows several number of clusters, derived from the non-uniform sampling of the CC. Running the k-means clustering algorithm in order to find 3 clusters in this embedding, gives raise to a *clustering artifact* which is referred as *incomplete clustering* in [Moberts *et al.*, 2005]

4.1.2 Real data

In this section the spectral clustering algorithms are applied to a simple real dataset in order to exhibit the artifacts in the results. The dataset is taken from the *Slicer user training 101* webpage, http://wiki.na-mic.org/Wiki/images/7/72/Tensor_data

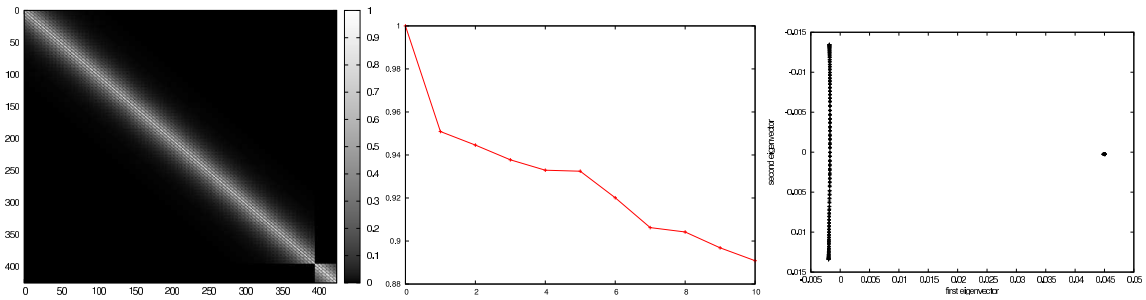

(a) affi nity matrix (b) biggest eigenvalues (c) 2D embedding

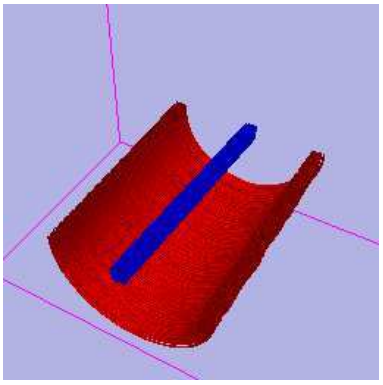

(d) clustering results

Figure 11: From left to right, the affinity matrix for the tracts shown in figure 10 generated with a kernel with parameter $\sigma = 2$, the biggest 10 eigenvalues of the affinity matrix and the 2D normalized embedding space. Observing the eigenvalues plot, the number of clusters to be found is two and it can be noted that simple clustering methods, as k-means, will succeed performing the clustering of these elements.

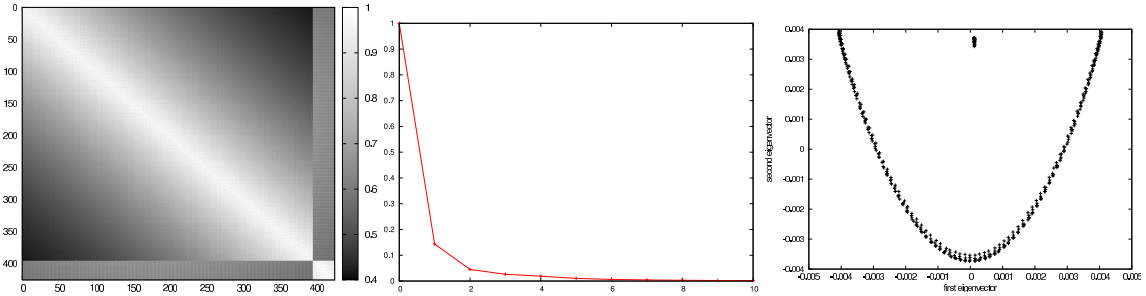

(a) affi nity matrix (b) biggest eigenvalues (c) 2D embedding

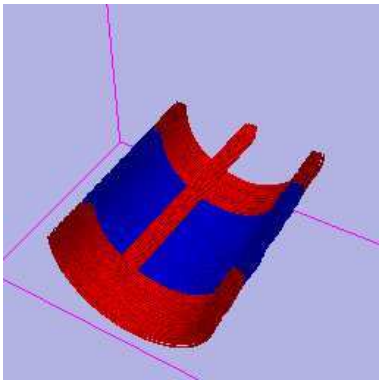

(d) clustering results

Figure 12: From left to right, the affinity matrix for the tracts shown in figure 10 generated with a kernel with parameter $\sigma = 10$, the biggest eigenvalues not counting of the affinity matrix and the 2D normalized embedding space. Observing the eigenvalues plot, the number of clusters to be found is still two, but it can be noted that k-means clustering, *will not* succeed performing the clustering of these elements. Nor will any algorithm that performs clustering by linear separation of the domain.

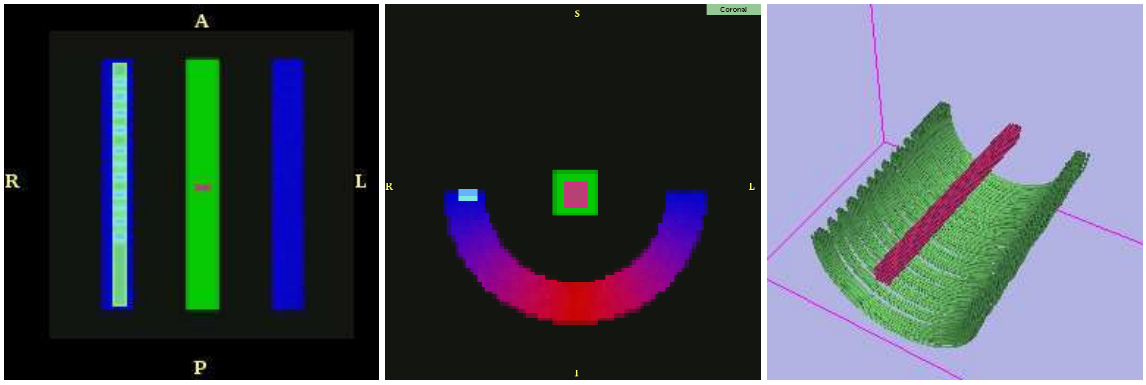

(a) axial (b) coronal (c) tractography

Figure 13: Regions of interest used to seed the tractographies shown in axial, (a), and coronal, (b), views, the light-green and cyan corresponding to the synthetic CC and the magenta one corresponding to the CG. The resulting tract bundles colored according to the regions, the cyan region of interest is not used as seed in order to obtain a non-uniform sampling of the CC (c).

synthetic data, two ROIs were set up in order to perform the tractography of the corpus callosum (CC) in cyan and the superior longitudinal fasciculus (SLF) in yellow. The ROIs and the manually colored tractographies are shown in figure 15.

As in section 4.1.1, the clustering algorithm is executed over the data shown in figure 15 taking $\sigma = 2$. The results of the embedding and clustering procedure are shown in figure 16. Observing the eigenvalues plot, it can be noticed that the number of clusters to be found is 3, while the expected number of clusters is 2. With respect to the embedding, it shows several number of clusters, derived from the non-uniform sampling of the fibers. Running the k-means clustering algorithm in order to find 3 clusters in this embedding, gives raise to a the *incomplete clustering* artifact *clustering artifact* as exhibited in section 4.1.1. In order to show the non-uniform block structure of the clusters, the affinity matrix was reordered using the second eigenvector following [Behrens, 2004, section 7.2.2].

4.2 Avoiding the artifacts

In the previous section, it was pointed out that unless all the elements of each cluster are uniformly sampled, this cluster will be teared apart in several clusters due to the existence of a non-constant increment in the approximation of the Laplacian which depends on the sampling frequency. Moreover, practical consequences of this problem were shown on synthetic data in section 4.1.1. In order to solve this problem, we apply the prenormalization presented in section 3 corresponding to the diffusion maps technique

The results of applying this normalization to the data given in section 4.1.1 are shown in figure 17. In the eigenvalue plot, figure 17(b), it can be noted that there are two clusters, which can be separated easily in the embedding shown in

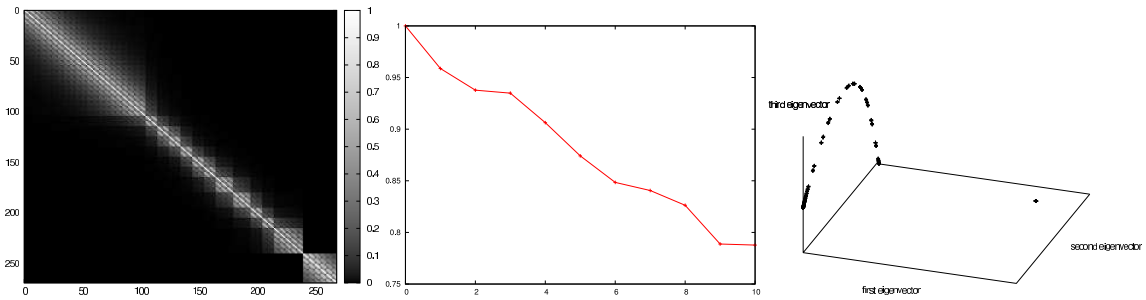

(a) affi nity matrix (b) biggest eigenvalues (c) 3D embedding

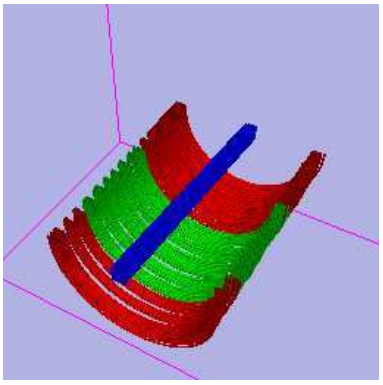

(d) clustering result

Figure 14: From left to right, the affinity matrix for the tracts shown in figure 13 generated with a kernel with parameter $\sigma = 2$, the biggest 10 eigenvalues of the affinity matrix and the 3D normalized embedding space. Observing the eigenvalues plot, it can be noticed that the number of clusters found is 3, while the expected number is two, one for the artificial CG simulation and one for the artificial CC. The result of the clustering is shown in (d).

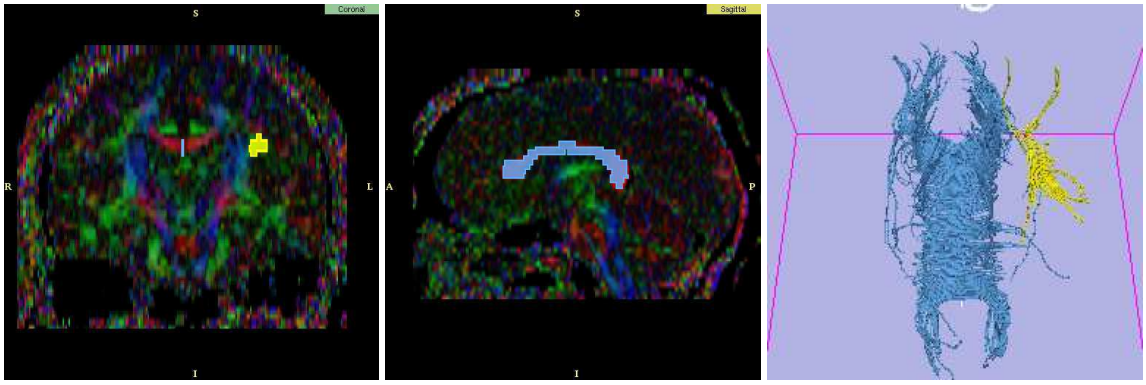

(a) coronal (b) saggital (c) tractography

Figure 15: Real data tractography, from left to right, the coronal and saggital views with the regions of interest corresponding to the corpus callosum (CC) in cyan and the superior longitudinal fasciculus (SLF) in yellow; finally, the tractography, manually colored according to the ROI colors.

figure 17(c), pay special attention to the scale difference between the edges. Finally the expected clustering is exhibited in figure 17(d), showing the same clustering as in the manually colored bundles figure 10.

Furthermore, the results of applying the same procedure to the real data set presented in section 4.1.2, taking $\sigma = 5$, are shown in figure 18[3]. In the eigenvalue plot, figure 18(b), it can be noted that there are two clusters, which can be separated easily in the embedding shown in figure 18(c). Finally the correct clustering is exhibited in figure 18(d). In order to show the block structure of the affinity matrix, it is shown reordered using the second eigenvector in figure 18(e) as shown in [Behrens, 2004, section 7.2.2].

4.3 Clustering fibers emanating from the cerebral cortex

Diffusion weighted data was acquired from a 1.5 Tesla GE Signa at the Centre Hospitalier National d'Ophtalmologie des Quinze-Vingts, Paris, France. The spin-echo echo-planar imaging sequence, TE= 91.8 ms, TR = 5 s, 128 x 128 image matrix, FOV = 203x203 mm^2 with a b-value of 1000 s/mm^2. The measurement of 36 slices with 3.5 mm thickness covered the whole brain. Acquisition time was 14 minutes. From [Jbabdi, 2006], 574 points were taken on the cerebral cortex. Streamline tractography was done seeding from each of these points and finally our spectral clustering and embedding algorithm was applied to these fiber tracts. Results are shown in figure 19. It can be seen that our algorithm was able to distinguish between different sets of associative fiber within each lobe (cyan, orange, yellow), the projection fibers connecting the cortex to the thalamus (blue) and two bundles of commisural fibers, the anterior and posterior commisures (green, red).

[3] In section 4.1.2 the parameter is $\sigma = 2$, nevertheless the results are even worst as the embedding space exhibits non-separable clusters.

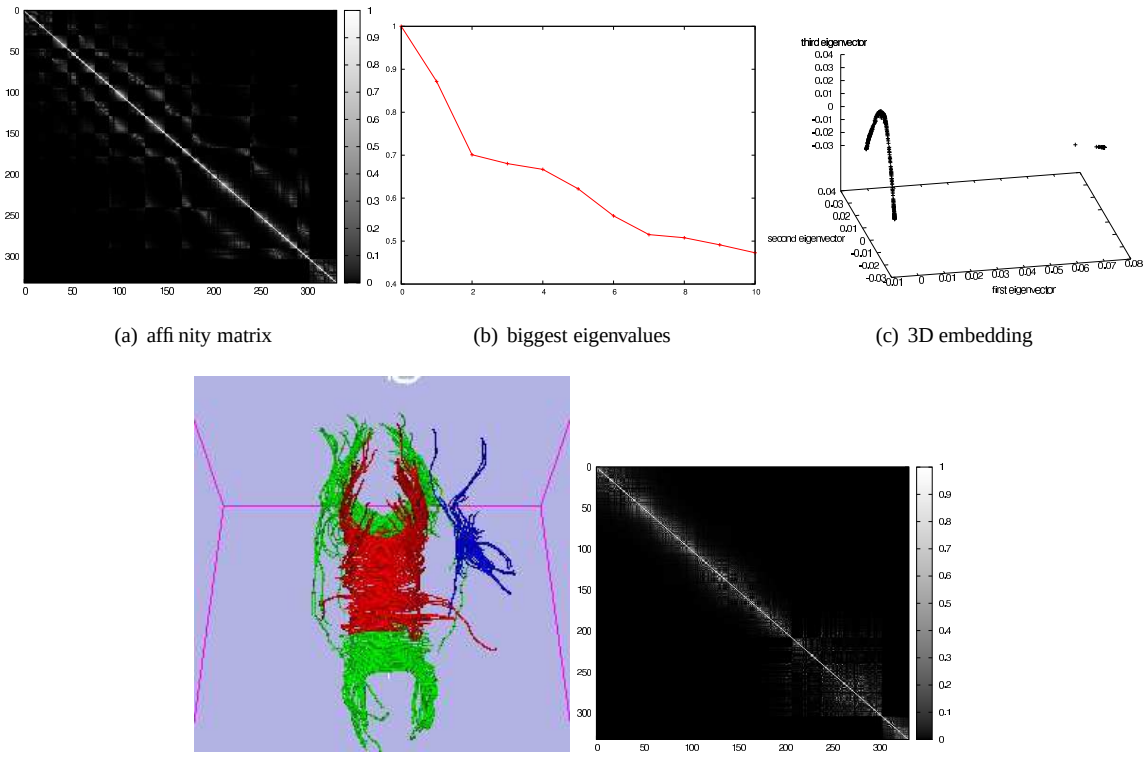

(a) affi nity matrix (b) biggest eigenvalues (c) 3D embedding

(d) clustering result (e) reordered affi nity matrix

Figure 16: From left to right, the affinity matrix for the tracts shown in figure 15 generated with a kernel with parameter $\sigma = 2$; the biggest 10 eigenvalues; the 3D normalized embedding space. Observing the eigenvalues plot, it can be noticed that the number of clusters to be found is 3. The result of the clustering is shown in (d) and the reordered affinity matrix in (e).

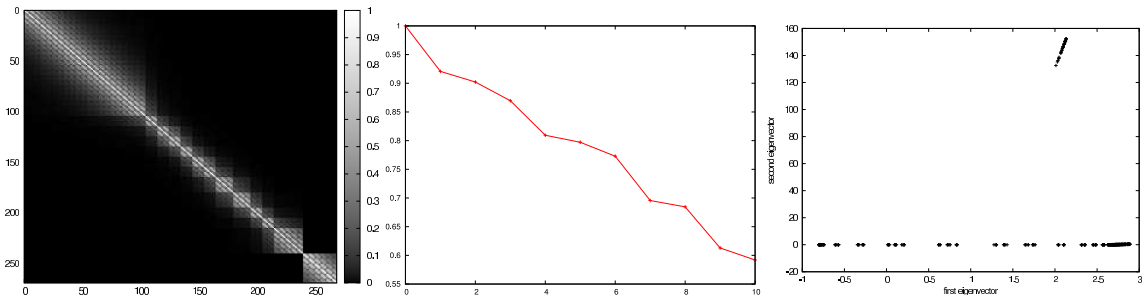

(a) affi nity matrix (b) biggest eigenvalues (c) 3D embedding

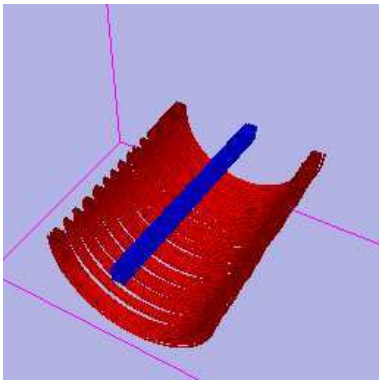

(d) clustering result

Figure 17: From left to right, the affinity matrix for the tracts shown in figure 13 generated with a kernel with parameter $\sigma = 2$; the biggest 10 eigenvalues of the affinity matrix that was prenormalized in order to avoid sampling frequency dependant artifacts; the 2D normalized embedding space. The result of the clustering, where the number of clusters shown by the eigenvalue plot is 2, is shown in (d).

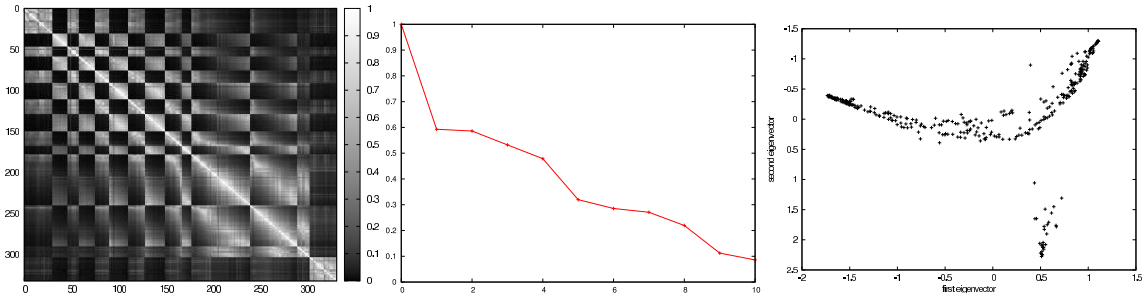

(a) affi nity matrix (b) biggest eigenvalues (c) 3D embedding

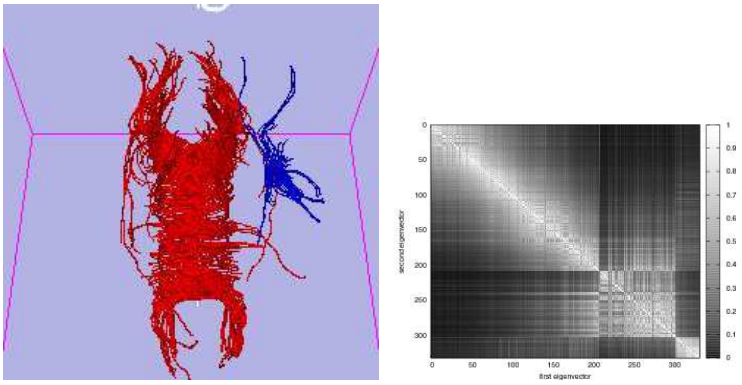

(d) clustering result (e) reordered affi nity matrix

Figure 18: From left to right, the affinity matrix for the tracts shown in figure 15 generated with a kernel with parameter $\sigma = 5$; the biggest 10 of the affinity matrix prenormalized in order to avoid sampling frequency dependant artifacts; the 2D normalized embedding space. Observing the eigenvalues plot, it can be noticed that the number of clusters to be found is 3. The result of the clustering is shown in (d) and the reordered affinity matrix in (e).

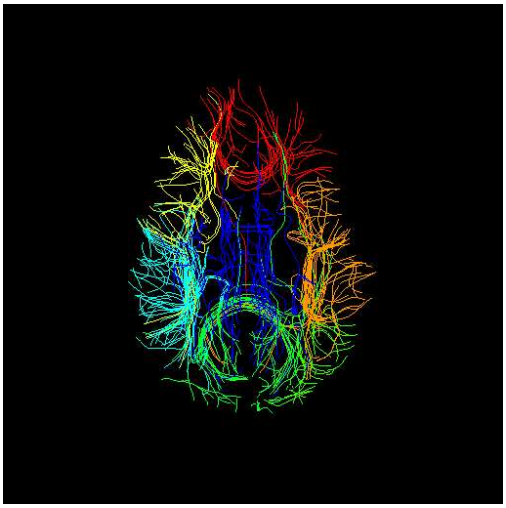

Figure 19: Real data results on streamline tractography emanating from 574 points in the cerebral cortex. Each cluster is colored differently. It can be seen that our algorithm was able to distinguish between different sets of associative fiber within each lobe (cyan, orange, yellow), the projection fibers connecting the cortex to the thalamus (blue) and two bundles of commisural fibers, the anterior and posterior commisures (green, red).

5 Fiber bundle identification through Diffusion MRI segmentation

We now want to obtain the white matter fiber bundles through segmentation of Q-Ball images. In this work we achieve the segmentation through spectral clustering. These techniques have been successfully applied to image processing since [Shi and Malik, 2000], providing a method for image processing which involves manifold learning and it is initialization free. In order to achieve this, a metric between Q-Ball ODFs is needed. Which metric should be used on Q-Ball image analysis and clustering is still an open metric. Here, we describe a clustering algorithm that infers an embedding and a metric to compare ODF images. We derive an affinity measure incorporating the Euclidean distance and the spatial location distance between ODFs.

5.1 Diffusion Weighted Data Generation and Acquisitions

Synthetic Data We generate synthetic HARDI data using the multi-tensor model which is simple and leads to an analytical expression of the ODF [Descoteaux *et al.*, 2006a; Tuch, 2004a]. For a given b-factor and noise level, we generate the diffusion-weighted signal

$$S(\mathbf{u}_i) = \sum_{k=1}^{n} \frac{1}{n} \exp(-b\mathbf{u}_i^{\mathrm{T}} \mathbf{D}_{\mathbf{k}}(\theta)\mathbf{u}_i) + noise \tag{25}$$

where $\mathbf{u}_i$ is the ith gradient direction on the sphere, n is the number of fibers and $1/n$ is the volume fraction of the of each fiber. In practice, we use $N = 81$ from a 3^{rd} order tessellation of the icosahedron, $b = 3000$ s/mm^2 and $n = 1$ or 2. $\mathbf{D}_{\mathbf{k}}(\theta)$ is the diffusion tensor with standard eigenvalues $[3,3,1.7]$x10^{-2} mm^2/s oriented in direction θ, which agree

with reported physiological values [Pierpaoli *et al.*, 1996]. Finally, we add complex Gaussian noise with standard deviation of $1/35$, producing a signal with signal to noise ratio (SNR) of 35.

We generate three synthetic data example, two simple examples, one with a ring of sinusoidal shaped fibers, one with fibers with different sizes and scales and the other with complex crossing areas simulating the 'U'-fibers (cortico-cortical fibers) that can occur in the brain. These synthetic datasets help understand the behavior of the different spectral clustering methods when confronted with simple and complex fiber geometries.

Human Brain Data Diffusion weighted data and high-resolution T1-weighted images were acquired on a whole-body 3 Tesla Magnetom Trio scanner (Siemens, Erlangen) equipped with an 8-channel head array coil [Anwander *et al.*, 2007]. The spin-echo echo-planar-imaging sequence, TE = 100 ms, TR = 12 s, 128 x 128 image matrix, FOV = 220 x 220 mm^2, consists of 60 diffusion encoding gradients [Jones *et al.*, 1999] with a b-value of 1000 s/mm^2. Seven images without any diffusion weightings are placed at the beginning of the sequence and after each block of 10 diffusion weighted images as anatomical reference for offline motion correction. The measurement of 72 slices with 1.7mm thickness (no gap) covered the whole brain. Random variations in the data were reduced by averaging 3 acquisitions, resulting in an acquisition time of about 45 minutes. No cardiac gating was employed to limit the acquisition time. The issue of cardiac gating is discussed in [Jones *et al.*, 2002]. Additionally, fat saturation was employed and we used 6/8 partial Fourier imaging, a Hanning window filtering and parallel acquisition (generalized auto-calibrating partially parallel acquisitions, reduction factor = 2) in the axial plane.

The brain is peeled from the T1-anatomy, which was aligned with the Talairach stereotactical coordinate system [Talairach and Tournoux, 1988]. The 21 images without diffusion weightings distributed within the whole sequence were used to estimate motion correction parameters using rigid-body transformations [Jenkinson *et al.*, 2002], implemented in [FSL, 2006]. The motion correction for the 180 diffusion-weighted images was combined with a global registration to the T1 anatomy computed with the same method. The gradient direction for each volume was corrected using the rotation parameters. The registered images were interpolated to the new reference frame with an isotropic voxel resolution of 1.72 mm and the 3 corresponding acquisitions and gradient directions were averaged.

5.2 Spectral embedding and clustering

Distance Functions Between Elements to Cluster In order to implement the Diffusion Maps spectral clustering method a distance function for each data type is chosen. This distance function is used to calculate the affinity matrix as expressed by equation (19). In the DT case we use the tensor distance shown in equation (9). In the ODF case we use the distance shown in equation (14).

Affinity matrix construction Each element of a DT or a ODF image can be represented as having two components. In the DT case $(\mathbf{x}, \mathbf{D})$, where $\mathbf{x} \in \mathbb{R}^3$ is the position in the image and $\mathbf{D} \in \mathbb{R}^{3\times3}$ symmetric, positive definite. In the Q-Ball case, $(\mathbf{x}, \Psi)$, where $\Psi \in \mathbb{R}^L$ are the spherical harmonic coefficients. In both cases there is two kinds of information

to be taking in account, the positional one and the representing the diffusion at each position. Both information kinds need to be taking in account differently, in the image segmentation case [Shi and Malik, 2000] do it by taking, as a distance, a weighted sum of two separate distances, in this case the positional and the diffusivity one, but this adds a parameter to the algorithm and the way of mixing both distances is not intuitive. In this work, we chose a random walk based technique. This technique is more cohesive with the spectral embedding approach, which has been related with random walks in [Lafon and Lee, 2006]. Following [Tishby and Slonim, 2000; Ziyan *et al.*, 2006], we use the affinity between the elements in two neighboring voxels as a way to calculate the probability of a random walker going from one voxel to the other. Then a matrix relating only neighboring voxels through its walking probability can be built as,

$$\{A_1\}_{ij} = \begin{cases} a(x_i, x_j)) & \text{if } \| \text{coords}(x_i) - \text{coords}(x_j) \|_2 \leq 1 \\ 0 & \text{any other case} \end{cases}$$

where x_i, x_j is the diffusivity part- $\mathbf{D}$ or Ψ -of the two elements to be clustered, $a(x_i, x_j)$ is defined as in equation (19), and coords(x_i) are spatial coordinates of element x_i in the image. In order to turn the affinities into probabilities, the matrix A^1 must be normalized,

$$P = \frac{1}{\max_l D(A_1)_{ll}} \begin{cases} \max_l D(A_1)_{ll} - D(A_1)_{ii} & \text{if } i = j \\ \{A_1\}_{ij} & \text{any other case} \end{cases},$$

where diagonal adjustment forces the inherent random walk to a uniform steady state, hence every part of the Markov field will be explored at the same speed. Then, $(P_{ij})^s, s\{1,2,\ldots\}$ represents the probability of arriving to the voxel coords(x_j), starting from coords(x_i) through walking s steps.

In order to illustrate this, we show a simple example with a scalar image. The affinity is calculated as $a(x_i, x_j)$, where the distance is the absolute difference between the intensity on the image. The scalar image is figure 20(a), the probabilities of reaching other voxels in the image with one step starting from a voxel in the edge of the circle are shown in figure 20(b). As each voxel is an element of X, this is equivalent as calculating P for the image and taking P_{ij} as the probability of starting in i and reaching j, thus figure 20(b) is obtained by mapping the matrix row P_i to a bi-dimensional image. Finally, the probabilities of reaching every voxels in the image by taking 18 and 60 steps starting from a voxel in the edge of the circle are shown in figure 20(c) and figure 20(d), where the values are taken from the matrix P^{18} and P^{60} respectively.

Finally the matrix P^s is taken as the input for the diffusion maps embedding process described in section 3. The quanta of steps s is chosen to be the smallest integer where P^s does not have any element with a value of 0, giving in this way the weakest connected random walk over the whole image.

5.3 Synthetic data experiments

Diffusion Maps vs. N-Cuts The first experiment shows the difference in performance between the Diffusion Maps and N-Cuts approach. The N-Cut algorithm does not perform the sampling-based normalization described by equation (23) and is thus sensitive to sampling frequency differences within the clusters. In order to show this sampling

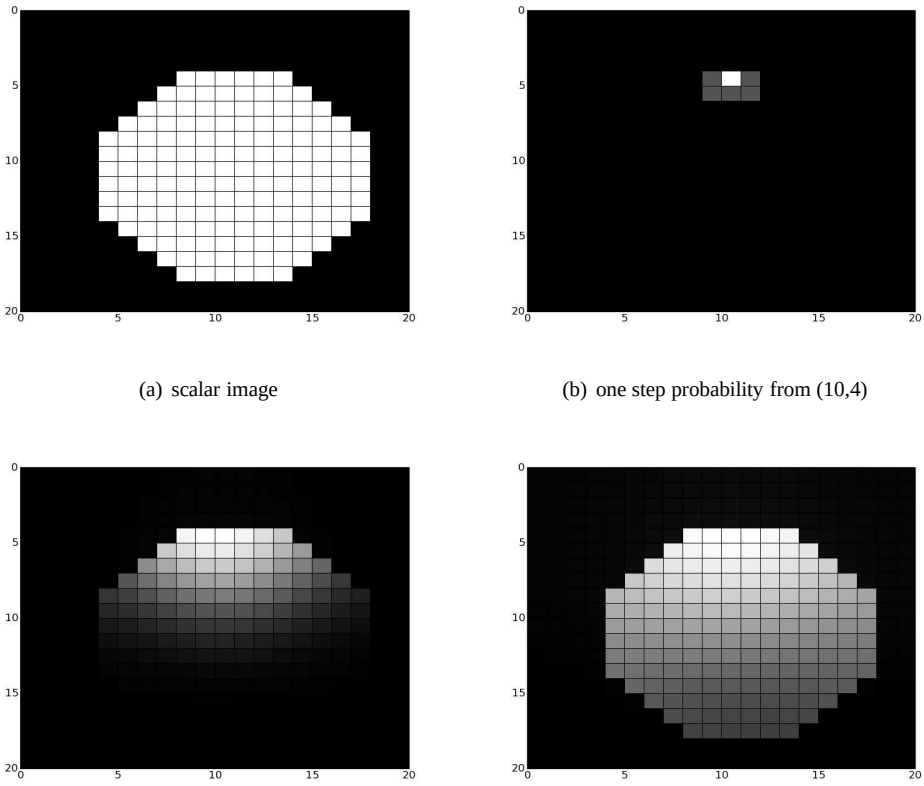

(a) scalar image

(b) one step probability from (10,4)

(c) eighteen steps probability from (10,4)

(d) sixty steps probability from (10,4)

Figure 20: Markovian relaxation to calculate connectivity in an image. From a scalar image figure 20(a), the probabilities of reaching other voxels in the image with one step starting from a voxel in the edge of the circle are shown in figure 20(b). Then the probabilities of reaching other voxels in the image with 18 steps starting from a voxel in the edge of the circle are shown in figure 20(c) and with 60 steps figure 20(d)

hypothesis problem, we used a ring fiber bundle with different sampling frequencies. Within the ring, the fibers have a sinusoidal shape and the frequency of the modulating sine function is 4 times bigger in the lower half of the ring. More formally, the fibers follow the angular function $o(\theta) = \theta + \frac{1}{8}\pi \sin(\mu \cdot \theta), 0 \leq \theta < 2\pi$, where $\mu = 8$ for the upper half of the ring and $\mu = 32$ for the lower half. Two clusters are expected, the ring and the background. The results of both clustering techniques are shown in figure 21, where the background has been masked out. Figure 21(a) shows the plot of the first 10 eigenvalues for the N-Cuts method, shown in figure 21(b) and figure 21(c). The slope between the line joining λ_0 and λ_1 and the line joining λ_1 and λ_2 changes drastically. This elbow at λ_1 indicates that there are 2 clusters. Figure 21(d) shows the plot of the first 10 eigenvalues for the Diffusion Maps method whose clustering results are shown in figure 21(e). The N-Cuts exhibits frequency-dependent clustering artifacts while the Diffusion Maps method clearly shows two clusters. In the Diffusion Maps, the clustering has correctly segmented the background and the ring.

ODF vs. DT images In figure 22, a single fiber scenario with no fiber crossing is shown. The DT-based and ODF-based image clustering produce the same results. Hence, ODF clustering reproduces DT-based results on a simple fiber population example.

Finally, figure 23 shows a fiber crossing scenario with two overlapping fiber bundles that have different geometries. Segmentation was performed over the DT and the ODF image shown in figure 24. Note that the cluster number is correctly estimated only in the ODF image. Moreover, the ODF N-Cuts segmentation exhibits artifacts not present in the ODF Diffusion Maps segmentation. The ODF Diffusion Maps effectively identify the two different fiber bundles as well as the fiber crossing areas.

5.4 Real Data

The real data experiment presented in this section shows the segmentation and labeling of a cropped axial and coronal slice. The cropped slices were chosen by an expert in regions of known fiber crossings where the DT model is normally limited. The ROIs show intersection of several fiber bundles. Hence, our segmentation algorithm is confronted with elements that have different orientation and different diffusion characteristics.

In order to show that ODF data segments the white matter fiber bundles better than the DT data in real cases, we analyze the evolution of the affinity matrix as the scale space parameter changes in the axial cropped slice shown in figure 25. Affinity matrices were computed with varying scale space parameter between $\frac{1}{5}$, $\frac{1}{10}$, $\frac{1}{20}$ and $\frac{1}{40}$ of the quantity of elements ($|X|$) to cluster respectively. In order to show the block structure of the affinity matrices, they were reordered using the second (Fiedler) biggest eigenvector [Fiedler, 1975]. It can be seen in figure 26 that as the scale diminishes, the DT data shows a high correlation between all the elements of the slice. This makes clustering very difficult because the blocks are small and highly correlated. On the other hand, the ODF data shows a very clear block structure across all scales. This block structure shows a high correlation of the elements within each block and a low inter-block correlation, giving a much better input to the clustering algorithm than the DT data.

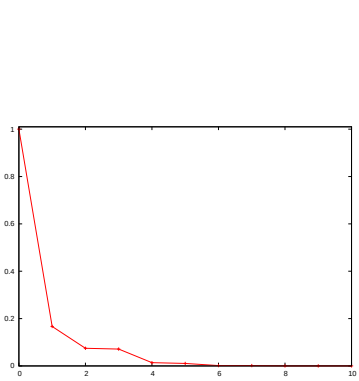

(a) N-Cuts eigenvalue plot

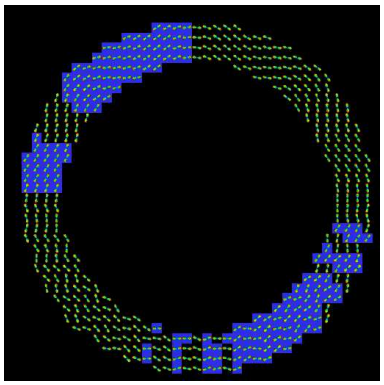

(b) N-Cuts, 2 clusters (blue and black)

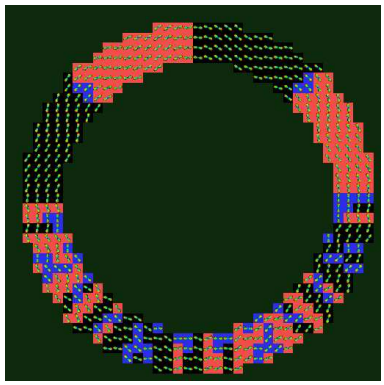

(c) N-Cuts, 3 clusters (blue, orange, black)

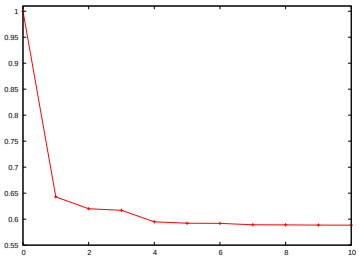

(d) Diffusion Maps eigenvalue plot

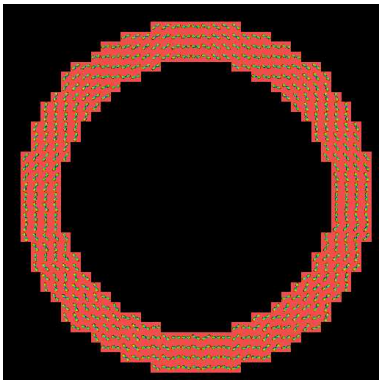

(e) Diffusion Maps, 2 clusters (orange and black)

Figure 21: N-Cuts generates over-clustering due to sampling frequency variation in ODF images. In both eigenvalue plots figure 21(a), figure 21(d), the slope between the line joining λ_0 and λ_1 and the line joining λ_1 and λ_2 changes drastically, expressing an elbow in λ_1, which indicates two clusters. The clustering results with 2, 21(b), and 3, 21(c), clusters are shown. Diffusion Maps correctly finds two clusters, the object and the background, 21(e). In the labeling, the ODFs are overlaid on the labels.

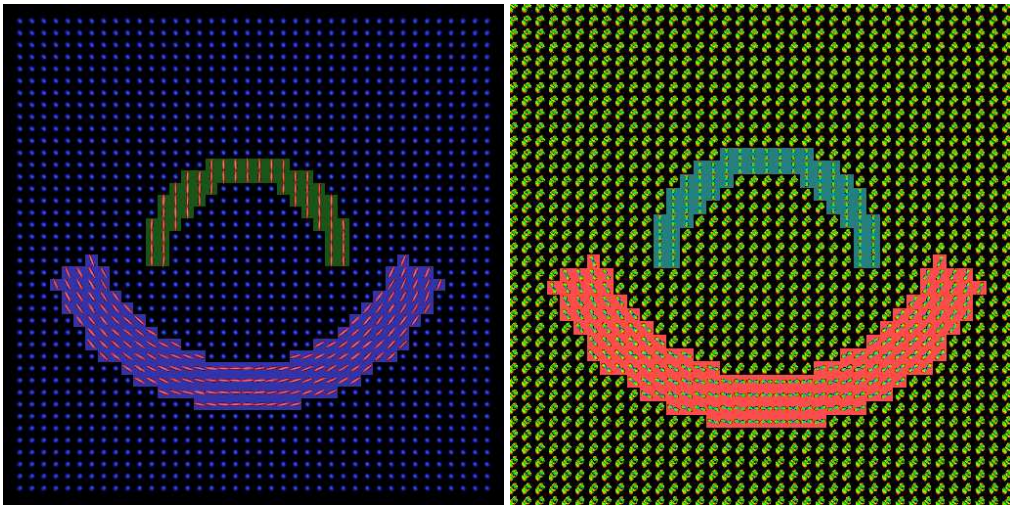

(a) DTI, 3 clusters (purple, green, black) (b) ODF, 3 clusters (orange, blue, black)

Figure 22: Synthetic image without fiber crossings. The results for the DT and ODF images are equivalent. The colors behind the DTs and ODFs indicate the clusters.

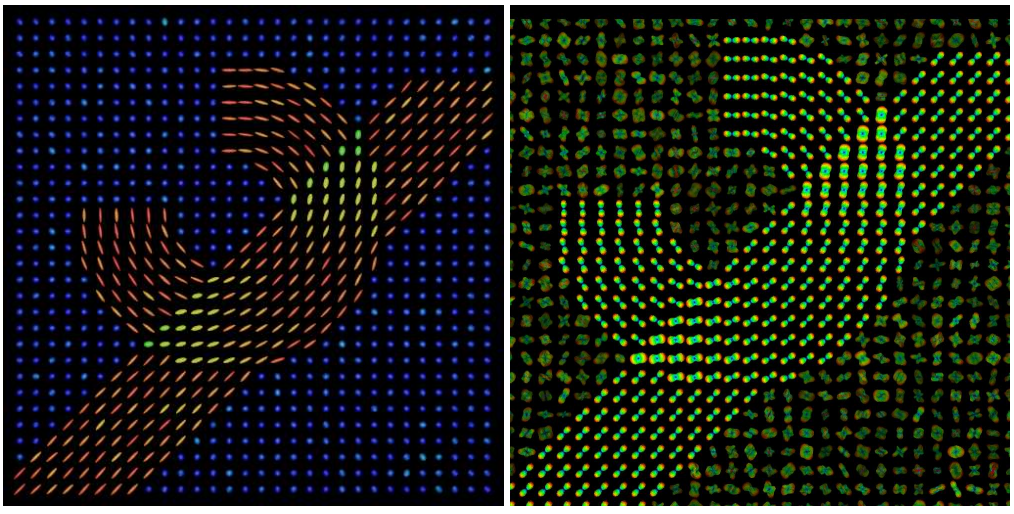

(a) DTI ellipsoids (b) ODF spherical functions

Figure 23: Synthetic DT and ODF images. The expected number is four, one for each fiber, one for the crossing between the two fibers and one for the background

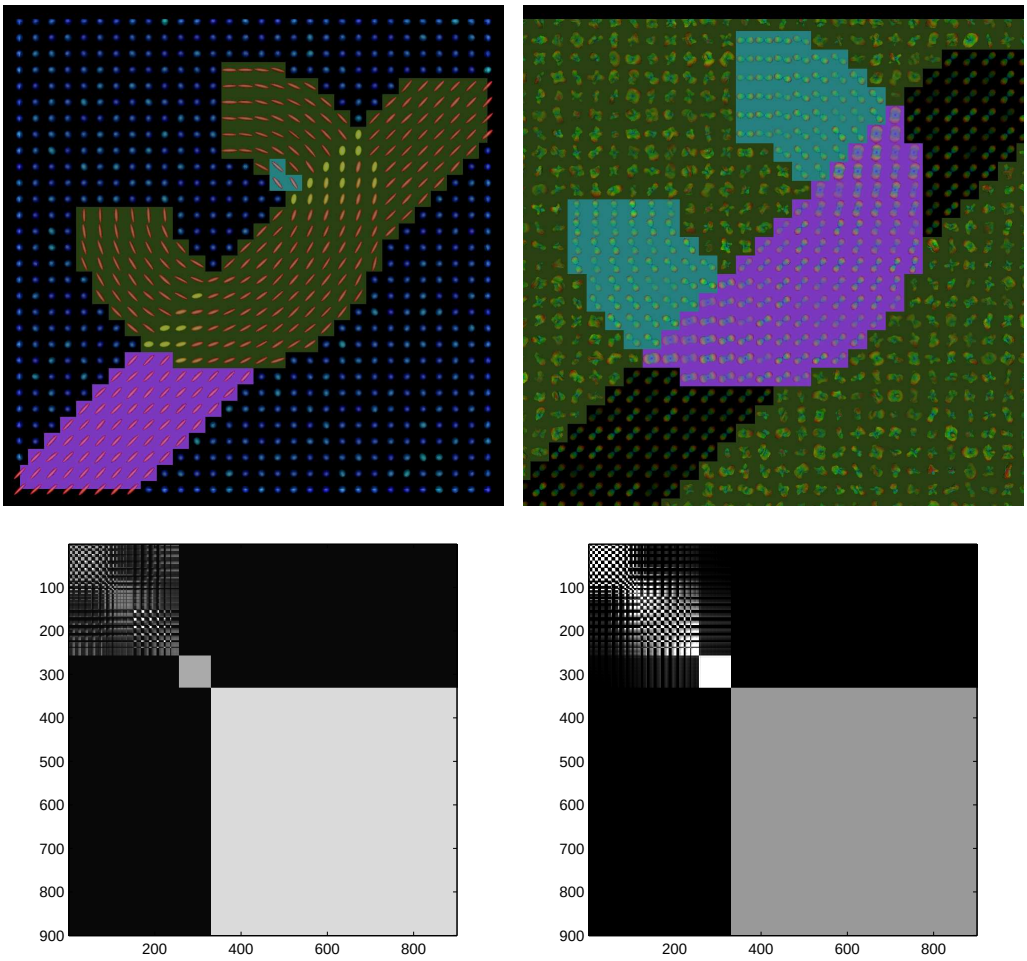

(a) DTI, 4 clusters (purple, green, blue, black)

(b) ODF, 4 clusters (black, purple, blue, green)

Figure 24: Clustering results in ODF and DT images, Only ODF show the correct clustering. In both cases the clustering result and the reordered affinity matrix are shown.

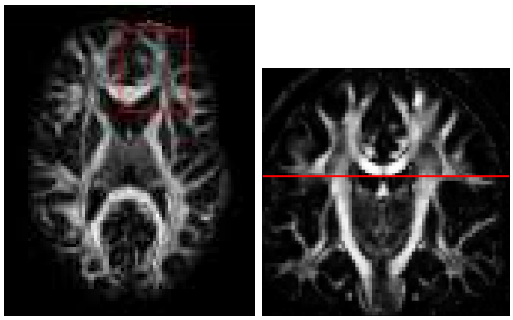

(a) Axial GFA slice with axial slice marked.

(b) Coronal GFA slice with cropped region marked.

Figure 25: Generalized fractional anisotropy axial, 25(a), and coronal, 25(b) slices in the real dataset.

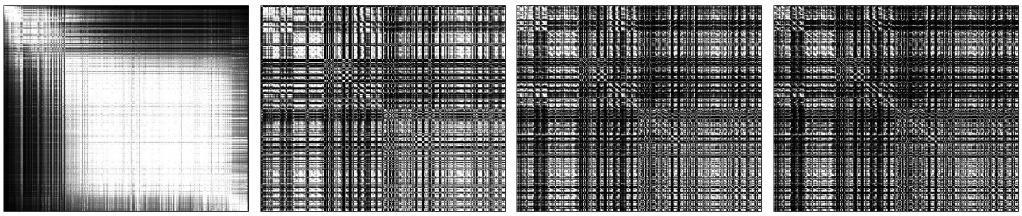

(a) DTI reordered affi nity matrices as the scale space parameter decreases

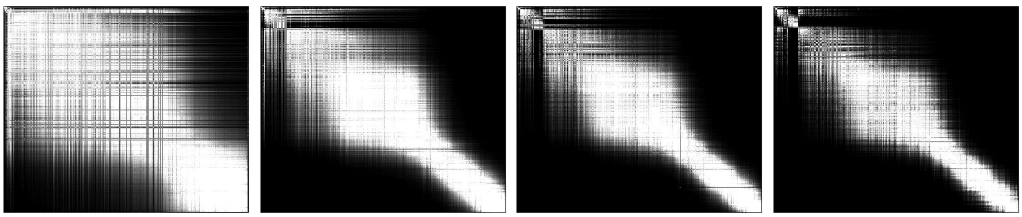

(b) ODF reordered affi nity matrices as the scale space parameter decreases

Figure 26: Plots of DTI and ODF affinity matrices of an axial cropped slice shown in figure 25. The matrices are reordered according to the second (Fiedler) eigenvector. The affinity matrices are shown in decreasing order of σ, which takes the values $\frac{1}{5}$, $\frac{1}{10}$, $\frac{1}{20}$ and $\frac{1}{40}$ of the quantity of elements to cluster. In the DTI case the decreasing on the scale parameter σ leads to a matrix with highly correlated elements that is very difficult to cluster. In the ODF case, the block structure is clear and is better suited to apply a clustering algorithm.

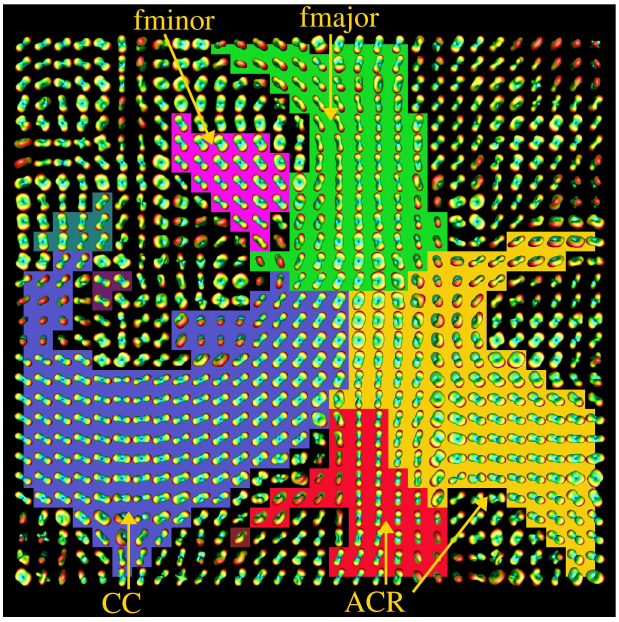

Figure 27: Our proposed algorithm is able to identify important white matter fiber bundles on an axial slice of a real dataset. The cropped axial slice shown in figure 25(a) has been segmented. In the labeled ODF visualization, each color represents one of the clusters found. The white matter labels are CC: Corpus Callosum, ACR: Anterior Corona Radiata, fmajor: Forceps Major and fminor: Forceps Minor.

In figure 25, the location of the cropped axial slice is shown in the axial slice, figure 25(a), and coronal slice, figure 25(b). As it can be seen in the segmented and labeled axial slice, figure 27, the segmentation also allows to identify and label some of the main white matter structures, Corpus Callosum (CC), Anterior Corona Radiata (ACR), Forceps Major (fmajor) and Forceps Minor (fminor).

In figure 28, the location of the cropped coronal slice is shown in the axial slice, figure 28(a), and coronal slice, figure 28(b). As it can be seen in the segmented and labeled coronal slice, figure 28(c), the segmentation allows to identify and label main white matter structures: Corpus Callosum (CC), Cingulum (CG), Corona Radiata (CR), Superior Longitudinal Fasciculus (SLF). Note that the segmentation is resilient to crossing areas such as seen at the interface between CR and CC.

6 Discussion

We have presented an algorithm to perform spectral embedding and clustering. This algorithm was applied to streamline fiber tracts and dMRI in order to recover white matter fiber bundles. In both cases the proposed method combines state-of-the-art dMRI reconstruction and state-of-the-art spectral clustering techniques. Our algorithm is initialization-free and has only two parameters. a scale-space parameter and the number of white matter structures (clusters) to

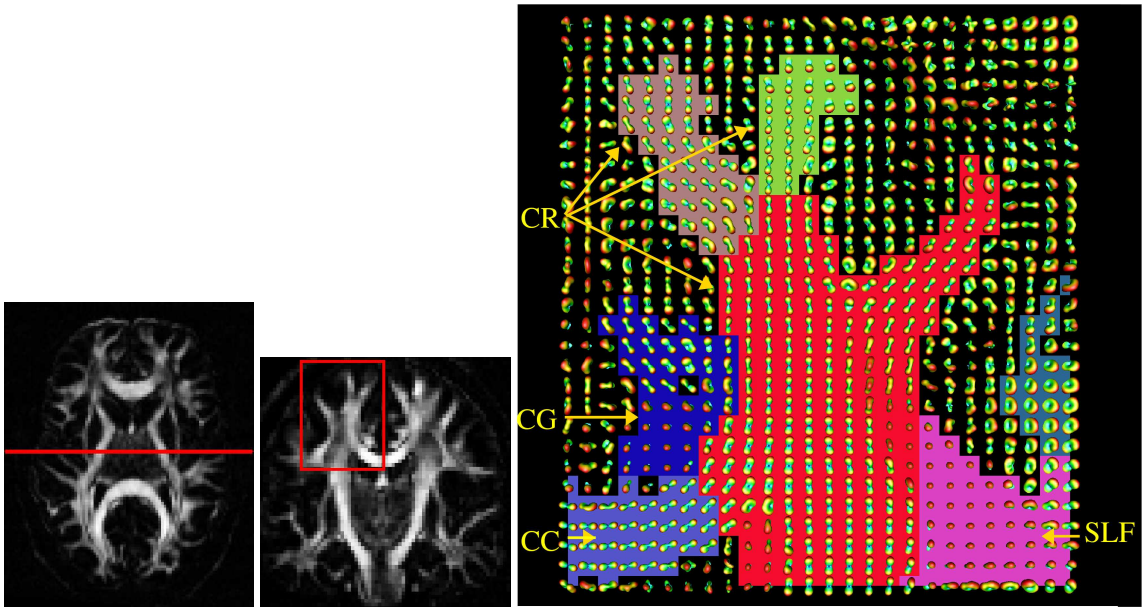

(a) Axial GFA slice with coronal slice marked.

(b) Coronal GFA slice with cropped region marked.

(c) Labeled ODF visualization of the cropped region.

Figure 28: Our proposed algorithm is able to identify important white matter fiber bundles on a coronal slice of a real dataset. Generalized fractional anisotropy axial, 28(a), and coronal, 28(b) slices are shown. Labeled ODF visualization, 28(c), each color represents one of the 7 clusters found. The white matter labels are CC: Corpus Callosum, CG: Cingulum, CR: Corona Radiata, SLF: Superior Longitudinal Fasciculus.

be found. Regarding this number of clusters parameter, we have proposed to estimate it automatically. We have introduced a spectral embedding technique that does not require uniform sampling of the elements. To apply spectral embedding and clustering techniques, we use a mean closest point based distance affinity metric between streamline fiber tracts. The affinity measure used for QBI incorporates an Euclidean distance measure between the spherical harmonic coefficients describing the q-ball ODFs and also incorporates the spatial location distance between ODFs. The affinity measure and the metric induced in the embedded space is then used to cluster fiber tracts and q-ball ODF images into multi-label segmentation representing the fiber bundles.

Spectral embedding has already been applied fiber tracts (e.g. [O'Donnell and Westin, 2006]) and to dMRI (e.g. [Ziyan *et al.*, 2006]). However, to our knowledge, this is the first work using the Diffusion Maps that avoids the high dependence on element sampling. It is also the first work attempting q-ball ODFs.

We have illustrated that when clustering dMRI images, the ODFs are the desirable elements to use for clustering in the white matter because the classical DT model is limited in regions of fiber crossings. The ODF is even more attractive because of the recent analytical spherical harmonic solution to the ODF reconstruction [Anderson, 2005; Descoteaux *et al.*, 2007; Descoteaux *et al.*, 2006b; Hess *et al.*, 2006]. The analytical solution is in fact as fast as a standard DT least-square estimation. In this work, we believe that we have used the state-of-the-art ODF reconstruction method [Descoteaux *et al.*, 2007], which is regularized, robust and very simple to implement.

The spectral embedding performed by the Diffusion Maps technique is at the heart of our segmentation algorithm. Whereas other spectral embedding techniques have a tendency to produce artifacts in the presence of different sampling characteristics within a cluster, the technique used in this work greatly reduces this tendency by performing the simple linear algebra calculation shown in equation (23).

Spectral embedding techniques produce a representation of the embedded data based on element-to-element affinities. This leads to the fundamental issue: how to choose the affinity measure? It is a challenge to find a measure that incorporates similarities between elements as well as the spatial location difference between elements. For similarities between elements, we chose a modified mean closest point distance between fiber tracts. Between q-ball ODFs we chose the Euclidean distance between spherical harmonic coefficients describing the ODFs. This approach is simple and very efficient because it allows to process the ODFs directly on the SH coefficients. The Euclidean distance has also been used successfully in a levelset segmentation framework [Descoteaux and Deriche, 2007] and it would be interesting to compare our spectral clustering approach against it. For spatial location difference in dMRI images, we chose Markovian Relaxation in order to be consistent with the graph theoretical representation of the Diffusion Maps technique. Although this way of representing the distance involves an artificial elimination of all the non-neighboring relations of the ODF elements in the affinity matrix and an adjustment of the diagonal elements, we believe that the resulting affinity relations represents the affinity better. The affinity of two neighboring elements at the beginning of the Markovian Relaxation algorithm is represented by a function of the Euclidean distance between them. This affinity can be interpreted as the probability that a random walker has of going from the first element to the second. The

affinity of two elements at the end of the relaxation is the probability of a random walker starting from one element and reaching the second in a certain number of steps.

The final step of our algorithm is k-means clustering. We believe that there is room for improvement in this last part of the algorithm. In the first place, the k-means algorithm needs an explicit number of clusters to find. This can be heuristically determined by analyzing the eigenvalue plot or the reordered affinity matrix structure, as shown in this work. However, an automatic method that could find the number of clusters would considerably improve the algorithm. In the second place, the k-means algorithm and its variants, for instance, k-medians search for isotropic clusters in the embedding space [Jain *et al.*, 1999]. These methods are able to perform clustering on convex structures. This could also improve the last clustering phase of our algorithm

Finally, in order to analyze the importance of the difference between our Diffusion Maps algorithm and the widely used N-Cuts, we used synthetic simulations. In these simulations, we generated a synthetic image with a single cluster within which the sampling of the elements changed. We showed that when this sampling changes, the N-cuts algorithm produces artifacts while our Diffusion Maps method does not. As uniform sampling within a cluster is a difficult property to guarantee in the white matter fiber bundles, our Diffusion Maps method is better suited for this task. We thus believe that Diffusion Maps are the right clustering method to be used on dMRI processing problems.

7 Conclusions

In this work, we have presented three contributions. First, a Diffusion Maps based technique for streamline fiber clustering and dMRI segmentation was developed to reduce artifacts arising from the widely used N-Cuts method. We have illustrated the advantages of the streamline fiber clustering and ODF Diffusion Maps segmentation algorithm, and showed on a real dataset that our algorithm is able to identify important and complex white matter fiber bundles.

Second, we have shown that in order to perform spectral clustering on complex dMRI with crossing fiber bundles, a HARDI technique such as Q-Ball Imaging is better than the classical DTI technique. This is because the ODF reconstructed from QBI is able to recover multiple crossing fiber distributions.

Finally, the Diffusion Maps technique has been shown to be more robust to sampling frequency variations within each object to be segmented. In order to cluster the elements, we have used an adaptive scale-space parameter and we have used Markovian Relaxation in order to incorporate spatial information. Overall, the approach is theoretically sound with the graph-based representation which lies at the heart of spectral clustering methods.

Therefore, we have an algorithm to perform fiber bundle clustering for a single brain, both in streamline fiber tracts and dMRI data. It is now important to study the behavior over several subjects in order to assess the reproducibility of the algorithm. In time, this will enable to perform multi-subject statistics within bundles in the embedded space. This will help characterize the white matter fiber bundles of several subjects and study if the alteration of these segmented tracts can provide new biomarkers for white matter diseases.

A The artifacts originated from non-uniform sampling (hypothesis 2).

In this section the origin of these artifact is first explained; then the use of a technique that relaxes the need of hypothesis 2, the diffusion maps [Coifman *et al.*, 2005], is presented. Finally the results of applying this technique are shown in synthetic and real data. In order to understand the origin of these artifacts, it is due to pay a special attention to the continuous setting of the manifold embedding problem.

A.1 Into the continuous, embedding a differentiable manifolds

In section 3, the process of embedding a set of elements X is defined as performing the eigenvalue decomposition (EVD) of the *laplacian* Δ *of the graph* $G(X,A)$. Where the graph $G(X,A)$ is conformed by a set of vertex elements X and a connectivity matrix A. As shown in section 3, this is done by calculating the laplacian of the graph,

$$\Delta = D(A) - A,$$

and then normalizing it

$$\tilde{\Delta} = D(\Delta)^{-\frac{1}{2}} \Delta D(\Delta)^{-\frac{1}{2}},$$

where

$$\{D(A)\}_{ij} = \begin{cases} \sum_k A_{ik} & i = j \\ 0 & i \neq j \end{cases}.$$

Then, a mapping $\mathbf{y}(X)$ onto an euclidean representation of X whose dimensionality n is smaller than the size of X, is defined by taking the first non-constant eigenvectors of $\tilde{\Delta}$ as the coordinated representation of each point.

Nevertheless, if the set that we want to embed is a Riemannian manifold, if instead of a set of elements X, we have a smooth, compact, N-dimensional manifold $\mathcal{M}$ with a distance function $\text{dist}_{\mathcal{M}} : \mathcal{M} \times \mathcal{M} \to \mathbb{R}$. Then graph representation is not appropriate due to its discrete nature..

The goal is to find, as we did with the graph, a mapping function $\mathbf{y} : \mathcal{M} \to \mathbb{R}^n, n \ll N$, which preserves the distances between the elements.

Following [Belkin, 2003, section 2.3.2], if the manifold $\mathcal{M}$ is isometrically embedded in $\mathbb{R}^N$, meaning,

$$\text{dist}_{\mathcal{M}}(\mathbf{x},\mathbf{z}) = \|\mathbf{x}-\mathbf{z}\|_{\mathbb{R}^N} + o\left(\|\mathbf{x}-\mathbf{z}\|_{\mathbb{R}^N}\right),\ \mathbf{x},\mathbf{z} \in \mathcal{M},$$

and the mapping $\mathbf{y}(\cdot)$ exists and is twice differentiable, then

$$\|\mathbf{y}(\mathbf{x}) - \mathbf{y}(\mathbf{z})\|_{\mathbb{R}^n} \leq \|\nabla f(\mathbf{x})\| \|\mathbf{x}-\mathbf{z}\|_{\mathbb{R}^N} + o\left(\|\mathbf{x}-\mathbf{z}\|_{\mathbb{R}^N}\right).$$

Thus, the gradient of the mapping, $\nabla f(\cdot)$, is a measure of how apart $\mathbf{y}(\cdot)$ maps nearby points of $\mathcal{M}$. Therefore the map that best preserves the locality on average is

$$f = \text{argmin}_{\|f\|_{L^2(\mathcal{M})}} \int_{\mathcal{M}} \|\nabla f\|^2.$$

By Stoke's theorem, if $\mathbf{V}$ is a vector field

$$\int_{\mathcal{M}} < \mathbf{V}, \nabla f >= - \int_{\mathcal{M}} \mathrm{div}(\mathbf{V}) f,$$

which takes us to

$$\int_{\mathcal{M}} \| \nabla f \|^2 = \int_{\mathcal{M}} < \nabla f, \nabla f >= \int_{\mathcal{M}} - \mathrm{div}(\nabla f) f,$$

where

$$\mathcal{L}(f) := - \mathrm{div}(\nabla f)$$

is called the *Laplace-Beltrami* operator over the manifold $\mathcal{M}$.

Hence, the mapping we are looking for is the function that minimizes the *Laplace-Beltrami* operator,

$$f = \mathrm{argmin}_{\| f \|_{L^2(\mathcal{M})}} \int_{\mathcal{M}} \mathcal{L}(f) f,$$

where $\mathcal{L}(f)$ is positive definite; moreover, according to [Rosenberg, 1997], if $\mathcal{M}$ is compact, $\mathcal{L}(f)$ has a discrete set of eigenvalues $0 = \lambda_0 \leq \lambda_1 \leq \cdots$ with its corresponding eigenfunctions $v^0(\cdot), v^1(\cdot), \cdots$ where $v^i : \mathcal{M} \rightarrow \mathbb{R}$. As in the graph setting, the eigenfunction $\mathbf{v}^0(\cdot)$ maps the entire manifold to one point, and the mapping, taken orthogonal to $\mathbf{v}^0(\cdot)$, into the euclidean space of $\mathbb{R}^n$ can be defined as

$$\mathbf{y}(\mathbf{x}) := (v^1(\mathbf{x}), \cdots, v^{n+1}(\mathbf{x})) \in \mathbb{R}^n, \mathbf{x} \in \mathcal{M} .$$

A.2 Back to the discrete, approximation of the *Laplace-Beltrami* operator

If we take X as a discrete sampling of elements from a manifold $\mathcal{M}$, then the *graph laplacian* of the graph $G(X,A)$ should be a *discrete approximation* of the *Laplace-Beltrami* operator over the manifold $\mathcal{M}$. Within this manifold, the distance for two elements $x_i, x_j \in X$ is $\mathrm{dist}_{\mathcal{M}}(\mathbf{x}_i, \mathbf{x}_j)$. Thus, noting the approximation of the Laplace-Beltrami operator as H,

$$Hf \propto \mathcal{L}(f).$$

Nevertheless it is shown in [Lafon, 2004, section 2.3.3], that if this approximation of the *Laplace-Beltrami*(LB) operator performed by the Laplacian Eigenmaps or N-Cuts algorithm actually has the form,

$$Hf \propto \mathcal{L}(f) + o\left(\left\langle \frac{\nabla p}{p}, \nabla f \right\rangle \right),$$

where $p(\cdot)$ is he probability density function of the sampling of the elements in X. This means that the approximation actually has the form "LB+potential"; where potential term depends on the probability distribution of the sampling X from the manifold $\mathcal{M}$, and becomes constant, thus unimportant, when this sampling is uniform. This leads to the artifacts exhibited in section 4.1.1 and section 4.1.2.

While this dependence on the distribution of the elements of X, which is a sampling of a real dataset, in the approximation of the LB operator is seen in [Brun *et al.*, 2003] as a way of enhancing the natural clusters in the data, this implies that *a difference in the sampling of X necessarily implies a different cluster in the real data set*, and this condition is not easy to guarantee, hence this property is proclive to span artifacts in the embedding.

References

[Anderson, 2005] A.W. Anderson. Measurements of fi ber orientation distributions using high angular resolution diffusion imaging. *Magnetic Resonance in Medicine*, 54:1194–1206, 2005. 7, 10, 43

[Anwander *et al.*, 2007] A. Anwander, M. Tittgemeyer, D. Y. von Cramon, A. D. Friederici, and T. R. Knosche. Connectivity-based parcellation of broca's area. *Cerebral Cortex*, 17(4):816–825, 2007. 33

[Arsigny *et al.*, 2006] Vincent Arsigny, Pierre Fillard, Xavier Pennec, and Nicholas Ayache. Log-Euclidean metrics for fast and simple calculus on diffusion tensors. *Magnetic Resonance in Medicine*, 56(2):411–421, August 2006. 7, 9

[Basser and Pierpaoli, 1996] P.J. Basser and C. Pierpaoli. Microstructural and physiological features of tissues elucidated by quantitative-diffusion-tensor MRI. *Journal of Magnetic Resonance B*, 111(3):209–219, 1996. 5, 12

[Basser *et al.*, 1994a] P.J. Basser, J. Mattiello, and D. LeBihan. Estimation of the effective self-diffusion tensor from the NMR spin echo. *Journal of Magnetic Resonance*, B(103):247–254, 1994. 6, 9

[Basser *et al.*, 1994b] P.J. Basser, J. Mattiello, and D. LeBihan. MR diffusion tensor spectroscopy and imaging. *Biophysical Journal*, 66(1):259–267, 1994. 5

[Basser *et al.*, 1994c] P.J. Basser, J. Mattiello, and D. LeBihan. MR diffusion tensor spectroscopy and imaging. *Biophysical Journal*, 66(1):259–267, 1994. 6, 9

[Basser *et al.*, 2000] P.J. Basser, S. Pajevic, C. Pierpaoli, J. Duda, and A. Aldroubi. In vivo fi ber tractography using DT-MRI data. *Magnetic Resonance in Medicine*, 44:625–632, 2000. 5, 11

[Basser *et al.*, 2002] Peter J. Basser, Sinisa Pajevic, Carlo Pierpaoli, and Akram Aldroubi. Fiber tract following in the human brain using dt-mri data. *IEICE TRANSACTIONS on Information and Systems (Special Issue on Measurements and Visualization Technology of Biological Information)*, E85-D(1):15–21, jan 2002. 11

[Behrens *et al.*, 2003a] T. E. J. Behrens, H. Johansen-Berg, M. W. Woolrich, S. M. Smith, C. A. M. Wheeler-Kingshott, P. A. Boulby, G. J. Barker, E. L. Sillery, K. Sheehan, and O. Ciccarelli. Non-invasive mapping of connections between human thalamus and cortex using diffusion imaging. *Nature Neuroscience*, 6:750–757, 2003. 5

[Behrens *et al.*, 2003b] T.E.J. Behrens, M.W. Woolrich, M. Jenkinson, H. Johansen-Berg, R.G. Nunes, S. Clare, P.M. Matthews, J.M. Brady, and S.M. Smith. Characterization and propagation of uncertainty in Diffusion-Weighted MR Imaging. *Magnetic Resonance in Medicine*, 50:1077–1088, 2003. 5

[Behrens, 2004] T.E.J. Behrens. *MR Diffusion Tractography: Methods and Applications*. PhD thesis, University of Oxford, 2004. 26, 28

[Belkin and Niyogi, 2003] Mikhail Belkin and Partha Niyogi. Laplacian eigenmaps for dimensionality reduction and data representation. *Neural Computation*, 15(6):1373–1396, jun 2003. 6, 15, 16, 17, 20, 23

[Belkin, 2003] Mikhail Belkin. *Problems of learning on manifolds*. PhD thesis, University of Chicago, aug 2003. 45

[Brand, 2003] Matthew Brand. Charting a manifold. Technical Report TR-2003-13, Mitsubishi Electric Research Labs, 2003. 6

[Brun *et al.*, 2003] A. Brun, H.J. Park, H. Knutsson, and C.F. Westin. Coloring of dt-mri fi ber traces using laplacian eigenmaps. In *Computer Aided Systems Theory - EUROCAST*, volume 2809 of *Lecture Notes in Computer Science*, pages 518–529. Springer, 2003. 12, 46

[Brun *et al.*, 2004] A. Brun, H.J. Park, H. Knutsson, M. E. Shenton, and C.F. Westin. Clustering fi ber traces using normalized cuts. In *Medical Image Computing and Computer-Assisted Intervention MICCAI 2004*, volume 3216 of *Lecture Notes in Computer Science*, pages 518–529. Springer/Verlag, 2004. 21, 23

[Campbell *et al.*, 2005] J.S.W. Campbell, K. Siddiqi, V.V. Rymar, A. Sadikot, and B.G. Pike. Flow-based fi ber tracking with diffusion tensor q-ball data: Validation and comparison to principal diffusion direction techniques. *NeuroImage*, 27(4):725–736, October 2005. 12

[Campbell, 2004] J. Campbell. *Diffusion Imaging of White Matter Fiber Tracts*. PhD thesis, McGill University, 2004. 7

[Castaño-Moraga *et al.*, 2007] CA Castaño-Moraga, C. Lenglet, R. Deriche, and J. Ruiz-Alzola. A Riemannian approach to anisotropic fi ltering of tensor fi elds. *Signal Processing*, 87(2):263–276, 2007.9

[Chung, 1997] F. Chung. *Spectral graph theory*. CBMS-AMS, 1997. 15, 18, 20

[Coifman *et al.*, 2005] R.R. Coifman, S. Lafon, A.B. Lee, M. Maggioni, B. Nadler, F. Warner, and S.W. Zucker. Geometric diffusions as a tool for harmonic analysis and structure defi nition of data: Diffusion maps. *Proceedings of the National Academy of Sciences*, 102(21):7426–7431, may 2005. 6, 16, 19, 20, 45

[Conturo *et al.*, 1999] T.E. Conturo, N.F. Lori, T.S. Cull, E. Akbudak, A.Z. Snyder, J.S. Shimony, R.C. McKinstry, H. Burton, and M.E. Raichle. Tracking neuronal fi ber pathways in the living human brain. *Proceedings of the National Academy of Sciences*, 96:10422–10427, August 1999. 5, 11

[Corouge *et al.*, 2005] Isabelle Corouge, P. Thomas Fletcherb, Sarang Joshic, Sylvain Gouttardd, and Guido Geriga. Fiber tract-oriented statistics for quantitative diffusion tensor mri analysis. In *Medical Image Analysis*, volume 10, pages 786–798, Oct 2005. The Eighth International Conference on Medical Imaging and Computer Assisted Intervention MICCAI 2005. 12

[Deriche and Descoteaux, 2007] Rachid Deriche and Maxime Descoteaux. Splitting tracking through crossing fi bers: multidirectional fi ber assignment by continuous tracking (M-FACT). In *International Symposium on Biomedical Imaging*, 2007. 12

[Descoteaux and Deriche, 2007] M. Descoteaux and R. Deriche. Segmentation of q-ball images using statistical surface evolution. In *Medical Image Computing and Computer Assisted Intervention*, Brisbane, Australia, Oct 2007. Springer. 43

[Descoteaux *et al.*, 2006a] M. Descoteaux, E. Angelino, S. Fitzgibbons, and R. Deriche. Apparent diffusion coeffi cients from high angular resolution diffusion imaging: Estimation and applications. *Magnetic Resonance in Medicine*, 56:395–410, 2006. 10, 22, 32

[Descoteaux *et al.*, 2006b] M. Descoteaux, E. Angelino, S. Fitzgibbons, and R.Deriche. A fast and robust odf estimation algorithm in q-ball imaging. In *Third IEEE International Symposium on Biomedical Imaging: from Nano to Macro*, pages 81–84, Arlington, Virginia, USA, April 2006. 43

[Descoteaux *et al.*, 2007] M. Descoteaux, E. Angelino, S. Fitzgibbons, and R. Deriche. Regularized, fast and robust analytical q-ball imaging. *Magnetic Resonance in Medicine*, 58:497–510, 2007. 5, 7, 10, 13, 43

[Donoho and Grimes, 2005] David L. Donoho and Carrie Grimes. Image manifolds which are isometric to euclidean space. *Journal of Mathematical Imaging and Vision*, 23:5–24, 2005. 15

[Fiedler, 1975] M. Fiedler. A property of eigenvectors of nonnegative symmetric matrices and its application to graph theory. *Czechoslovak Mathematical Journal*, 25:619–633, 1975. 20, 36

[Frank, 2002] Lawrence R Frank. Characterization of anisotropy in high angular resolution diffusion-weighted mri. *Magn Reson Med*, 47(6):1083–1099, Jun 2002. 13

[FSL, 2006] FSL. Fmrib software library. *University of Oxford*, 2006. 33

[Gray, 1918] Henry Gray. *Anatomy of the human body*. Philadelphia: Lea & Febiger, 1918; Bartleby.com, 2000, 1918. 5

[Hagmann *et al.*, 2006] Patric Hagmann, Lisa Jonasson, Philippe Maeder, Jean-Philippe Thiran, Van J. Wedeen, and Reto Meuli. Understanding diffusion mr imaging techniques: From scalar diffusion-weighted imaging to diffusion tensor imaging and beyond. *RadioGraphics*, 26:S205–S223, 2006. 12

[Hess *et al.*, 2006] C.P. Hess, P. Mukherjee, E.T. Han, D. Xu, and D.B. Vigneron. Q-ball reconstruction of multimodal fiber orientations using the spherical harmonic basis. *Magnetic Resonance in Medicine*, 56:104–117, 2006. 7, 10, 43

[Jain *et al.*, 1999] AK Jain, MN Murty, and PJ Flynn. Data clustering: a review. *ACM Computing Surveys (CSUR)*, 31(3):264–323, 1999. 15, 44

[Jbabdi, 2006] S. Jbabdi. *Modeling cerebral connectivity and low grade glioma invasion using diffusion tensor imaging*. PhD thesis, Ecole Centrale Paris, 2006. 28

[Jenkinson *et al.*, 2002] Mark Jenkinson, Peter Bannister, Michael Brady, and Stephen Smith. Improved optimization for the robust and accurate linear registration and motion correction of brain images. *NeuroImage*, 17(2):825–841, October 2002. 33

[Jolliffe, 1986] IT Jolliffe. *Principal component analysis*. Springer Series in Statistics, Berlin, 1986. 15

[Jonasson *et al.*, 2007] L. Jonasson, P. Hagmann, C. Pollo, X. Bresson, C.R. Wilson, R. Meuli, and J.P. Thiran. A level set method for segmentation of the thalamus and its nuclei in DT-MRI. *Signal Processing*, 87:309–321, 2007. Special Issue of Signal Processing on Diffuision Tensor Imaging. 9

[Jones *et al.*, 1999] D. K. Jones, M. A. Horsfield, and A. Simmons. Optimal strategies for measuring diffusion in anisotropic systems by magnetic resonance imaging. *Magnetic Resonance in Medicine*, 42:515–525, 1999. 33

[Jones *et al.*, 2002] D. K. Jones, S. C. R. Williams, D. Gasston, M. A. Horsfield, A. Simmons, and R. Howard. Isotropic resolution diffusion tensor imaging with whole brain acquisition in a clinically acceptable time. *Human Brain Mapping*, 15:216–230, 2002. 33

[Koch *et al.*, 2002] MA Koch, DG Norris, and M. Hund-Georgiadis. An Investigation of Functional and Anatomical Connectivity Using Magnetic Resonance Imaging. *NeuroImage*, 16(1):241–250, 2002. 5

[Lafon and Lee, 2006] S. Lafon and A.B. Lee. Diffusion maps and coarse-graining: a unified framework for dimensionality reduction, graph partitioning, and data set parameterization. *Pattern Analysis and Machine Intelligence, IEEE Transactions on*, 28(9):1393–1403, Sep 2006. 20, 23, 34

[Lafon, 2004] Setphane Lafon. *Diffusion Maps and Geometric Harmonics*. PhD thesis, Yale University, 2004. 16, 46

[Lazar and Alexander, 2005] M. Lazar and A. L. Alexander. Bootstrap white matter tractography (boot-tract). *NeuroImage*, 24:524–532, 2005. 5

[LeBihan and Breton, 1985] D LeBihan and E. Breton. Imagerie de diffusion *in vivo* par résonnance magnétique nucléaire. *CR Académie des Sciences*, (301):1109–1112, 1985. 5

[LeBihan *et al.*, 1986] D. LeBihan, E. Breton, D. Lallemand, P. Grenier, E. Cabanis, and M. Laval-Jeantet. MR imaging of intravoxel incoherent motions: Application to diffusion and perfusion in neurologic disorders. *Radiology*, 161(2):401–407, 1986. 5

[Lenglet *et al.*, 2006a] C. Lenglet, M. Rousson, and R. Deriche. DTI segmentation by statistical surface evolution. *Medical Imaging, IEEE Transactions on*, 25(6):685–700, June 2006. 11

[Lenglet *et al.*, 2006b] C. Lenglet, M. Rousson, R. Deriche, and 0. Faugeras. Statistics on the manifold of multivariate normal distributions: Theory and application to diffusion tensor mri processing. *Journal of Mathematical Imaging and Vision*, 25(3):423–444, October 2006. 12

[Lenglet *et al.*, 2006c] Christophe Lenglet, Mikaël Rousson, Rachid Deriche, and Olivier Faugueras. Statistics on the manifold of multivariate normal distributions: Theory and application to diffusion tensor mri processing. *J Math Imaging Vis*, 25:423–444, 2006. 7, 9, 11

[Lenglet, 2006] Christophe Lenglet. *Geometric and Variational Methods for Diffusion Tensor MRI Processing*. PhD thesis, I.N.R.I.A., 2006. 9

[Maddah *et al.*, 2005] M. Maddah, A. U. J. Mewes, S. Haker, W. E. L. Grimson, and S. K. Warfield. Automated atlas-based clustering of white matter fiber tracts from dtmri. In *Medical Image Computing and Computer-Assisted Intervention MICCAI 2005*, volume 3749 of *Lecture Notes in Computer Science*, pages 188–195. Springer Berlin / Heidelberg, 2005. 21, 23

[Merboldt *et al.*, 1985] K.D. Merboldt, W. Hanicke, and J. Frahm. Self-diffusion nmr imaging using stimulated echoes. *J. Magn. Reson.*, 64:479–486, 1985. 5

[Moberts *et al.*, 2005] B. Moberts, A. Vilanova, and J.J. van Wijk. Evaluation of fiber clustering methods for diffusion tensor imaging. In *Visualization, 2005. VIS 05. IEEE*, pages 65–72, 23-28 Oct. 2005. 23

[Mori and van Zijl, 2002] S. Mori and P. C. M. van Zijl. Fiber tracking: principles and strategies - a technical review. *NMR in Biomedicine*, 15:468–480, 2002. 11, 12

[Mori *et al.*, 1999] Susumu Mori, Barbara J. Crain, V. P. Chacko, and Peter C. M. Van Zijl. Three-dimensional tracking of axonal projections in the brain by magnetic resonance imaging. *Annals of Neurology*, 45(2):265–269, 1999. 5

[Nadler *et al.*, 2006] Boaz Nadler, Stephane Lafon, Ronald R. Coifman, and Ioannis G. Kevrekidis. Diffusion maps, spectral clustering and eigenfunctions of Fokker-Planck operators. In Y. Weiss, B. Schölkopf, and J. Platt, editors, *Advances in Neural Information Processing Systems 18*, pages 955–962. MIT Press, Cambridge, MA, 2006. 20

[O'Donnell and Westin, 2006] Lauren O'Donnell and Carl-Fredrik Westin. High-dimensional white matter atlas generation and group analysis. In Rasmus Larsen, Mads Nielsen, and Jon Sporring, editors, *MICCAI*, volume 4191 of *Lecture Notes in Computer Science*, pages 243–251. Springer, 2006. 12, 21, 23, 43

[O'Donnell, 2006] Lauren Jean O'Donnell. *Cerebral White Matter Analysis Using Diffusion Imaging*. PhD thesis, Massachusets Institute of Technology, May 2006. 22

[Parker and Alexander, 2003] G.J.M. Parker and D.C Alexander. Probabilistic monte carlo based mapping of cerebral connections utilising whole-brain crossing fibre information. In *IPMI*, pages 684–695, 2003. 5

[Pierpaoli *et al.*, 1996] C. Pierpaoli, P. Jezzard, P.J. Basser, A. Barnett, and G. Di Chiro. Diffusion Tensor MR imaging of human brain. *Radiology*, 201:637–648, 1996. 22, 33

[Prados *et al.*, 2006] E. Prados, S. Soatto, C. Lenglet, J.-P. Pons, N. Wotawa, R Deriche, and O. Faugeras. Control theory and fast marching techniques for brain connectivity mapping. In *IEEE Computer Society Conference on Computer Vision and Pattern Recognition*, 2006. 9

[Rosenberg, 1997] S. Rosenberg. *The Laplacian on a Riemannian Manifold: An Introduction to Analysis on Manifolds*. Cambridge University Press, 1997. 46

[Roweis and Saul, 2000] Sam T. Roweis and Lawrence K. Saul. Nonlinear Dimensionality Reduction by Locally Linear Embedding. *Science*, 290(5500):2323–2326, 2000. 14, 15

[Saul and Roweis, 2003] L.K. Saul and S.T. Roweis. Think Globally, Fit Locally: Unsupervised Learning of Low Dimensional Manifolds. *Journal of Machine Learning Research*, 4(2):119–155, 2003. 6

[Shi and Malik, 2000] Jianbo Shi and J. Malik. Normalized cuts and image segmentation. *Pattern Analysis and Machine Intelligence, IEEE Transactions on*, 22(8):888–905, Aug. 2000. 6, 15, 16, 17, 20, 23, 32, 34

[Stejskal and Tanner, 1965] E.O. Stejskal and J.E. Tanner. Spin diffusion measurements: spin echoes in the presence of a time-dependent field gradient. *Journal of Chemical Physics*, 42:288–292, 1965. 7

[Talairach and Tournoux, 1988] Jean Talairach and Pierre Tournoux. *Co-Planar Stereotaxic Atlas of the Human Brain: 3-Dimensional Proportional System : An Approach to Cerebral Imaging*. Thieme Medical Publishers, January 1988. 33

[Taylor and Bushell, 1985] D.G. Taylor and M.C. Bushell. The spatial mapping of translational diffusion coefficients by the nmr imaging technique. *Physics in Medicine and Biology*, 30(4):345–349, 1985. 5

[Tenenbaum *et al.*, 2000] J.B. Tenenbaum, V. Silva, and J.C. Langford. A Global Geometric Framework for Nonlinear Dimensionality Reduction. *Science*, 290(5500):2319, 2000. 14, 15

[Tishby and Slonim, 2000] Naftali Tishby and Noam Slonim. Data clustering by markovian relaxation and the information bottleneck method. In *Neural Information Processing Systems*, 2000. 34

[Tschumperlé and Deriche, 2003] D. Tschumperlé and R. Deriche. Variational frameworks for DT-MRI estimation, regularization and visualization. In *9*, pages 116–121, Nice, France, 2003. 7

[Tuch *et al.*, 2002] D.S. Tuch, T.G. Reese, M.R. Wiegell, N.G. Makris, J.W. Belliveau, and V.J. Wedeen. High angular resolution diffusion imaging reveals intravoxel white matter fiber heterogeneity. *Magn. Res. Med.*, 48(4):577–582, 2002. 7

[Tuch, 2004a] D. Tuch. Q-ball imaging. *Magnetic Resonance in Medicine*, 52(6):1358–1372, 2004. 5, 10, 11, 22, 32

[Tuch, 2004b] David S Tuch. Q-ball imaging. *Magn Reson Med*, 52(6):1358–1372, Dec 2004. 7

[Wang *et al.*, 2003] Z. Wang, B.C. Vemuri, Y. Chen, and T. Mareci. Simultaneous smoothing and estimation of the tensor field from diffusion tensor mri. In *IEEE Conference on Computer Vision and Pattern Recognition*, volume I, pages 461–466, Madison, Wisconsin (United States), June 2003. 7

[Wang *et al.*, 2004] Z. Wang, BC Vemuri, Y. Chen, and TH Mareci. A constrained variational principle for direct estimation and smoothing of the diffusion tensor field from complex DWI. *Medical Imaging, IEEE Transactions on*, 23(8):930–939, 2004. 11

[Weiss, 1999] Y. Weiss. Segmentation using eigenvectors: a unifying view. In *International Conference on Computer Vision*, volume 2, pages 975–982, 1999. 6, 15

[Westin *et al.*, 2002] C.F Westin, S.E Maier, H. Mamata, A. Nabavi, F.A. Jolesz, and R. Kikinis. Processing and visualization of diffusion tensor MRI. In *In proceedings of Medical Image Analysis*, volume 6(2), pages 93–108, 2002. 7

[Zelnik-Manor and Perona, 2004] L. Zelnik-Manor and P. Perona. Self-tuning spectral clustering. *Advances in Neural Information Processing Systems*, 17:1601–1608, 2004. 16

[Ziyan *et al.*, 2006] Ulas Ziyan, David Tuch, and Carl-Fredrik Westin. Segmentation of thalamic nuclei from dti using spectral clustering. In *Medical Image Computing and Computer-Assisted Intervention*, Lecture Notes in Computer Science, pages 807–814. Springer/Verlag, 2006. 6, 34, 43

Unité de recherche INRIA Sophia Antipolis

2004, route des Lucioles - BP 93 - 06902 Sophia Antipolis Cedex (France)

Unité de recherche INRIA Futurs : Parc Club Orsay Université - ZAC des Vignes

4, rue Jacques Monod - 91893 ORSAY Cedex (France)

Unité de recherche INRIA Lorraine : LORIA, Technopôle de Nancy-Brabois - Campus scientifi que

615, rue du Jardin Botanique - BP 101 - 54602 Villers-lès-Nancy Cedex (France)

Unité de recherche INRIA Rennes : IRISA, Campus universitaire de Beaulieu - 35042 Rennes Cedex (France)

Unité de recherche INRIA Rhône-Alpes : 655, avenue de l'Europe - 38334 Montbonnot Saint-Ismier (France)

Unité de recherche INRIA Rocquencourt : Domaine de Voluceau - Rocquencourt - BP 105 - 78153 Le Chesnay Cedex (France)

Éditeur

INRIA - Domaine de Voluceau - Rocquencourt, BP 105 - 78153 Le Chesnay Cedex (France)

http://www.inria.fr

ISSN 0249-6399